International Journal of Hydrogen Energy 103 (2025) 887–900

Contents lists available at ScienceDirect

International Journal of Hydrogen Energy

journal homepage: www.elsevier.com/locate/he

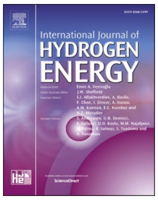

Unveiling the role of Ni nanometric particles in ultra-stable hierarchically porous Y zeolite to drive methane steam reforming and CO_2 hydrogenation

G. Sorbino [a], O. Tammaro [b], A. Padua [b], A. Basco [a], S. Scognamiglio [a,b], M. Sisti [c], R. Arletti [c], A. Marocco [d], M. Pansini [d], G. Landi [a,*], S. Esposito [b,**]

[a] *Institute of Science and Technology for Sustainable Energy and Mobility - CNR, Naples, Italy*
[b] *Dipartimento di Scienza Applicata e Tecnologia (DISAT), Politecnico di Torino, C.so Duca degli Abruzzi 24, 10129, Torino, Italy*
[c] *Chemical and Geological Sciences Department, University of Modena and Reggio Emilia, Via G. Campi 103, Modena, 41125, Italy*
[d] *Department of Civil and Mechanical Engineering and INSTM Research Unit, Università degli Studi di Cassino e del Lazio Meridionale, Via G. Di Biasio 43, Cassino, FR 03043, Italy*

ARTICLE INFO

Handling Editor: Dr F Gallucci

Keywords:
Ultrastable Y zeolites
Nickel-reduced species
Hierarchical porosity
Methane steam reforming
CO_2 hydrogenation

ABSTRACT

Three catalysts containing 5, 10 and 20 % wt. Ni trapped in the porous zeolite framework (Ni5, Ni10 and Ni20, respectively), were prepared. An ultra-stable zeolite Y, with a Si/Al molar ratio of 385, selected for its high thermal stability, was impregnated under vacuum with an aqueous solution of Ni^{2+} ions and thermally treated at 600 °C in a reducing atmosphere. The Ni nominal contents were compliant with the nominal value as confirmed by X-ray fluorescence spectroscopy. The catalysts were tested in the steam reforming of methane and in the hydrogenation of carbon dioxide. Catalytic activity is significantly structure-dependant.

Several physical-chemical characterizations were carried out. X-ray powder diffraction with synchrotron source, followed by Rietveld analysis, and H_2-TPR analysis indicate that all the loaded nickel is in the metallic form. High-resolution transmission electron microscopy showed that the particle size distribution is centred around 30 nm for Ni5 and Ni 10, while particles of around 150 nm are obtained with Ni20. A thorough NLDFT analysis of the pore size distribution shows a certain fraction of large mesoporosity in addition to the microporosity typical of zeolites. This hierarchical structure, also evidenced by the TEM micrographs, has a profound impact on the catalytic response since the nickel particles are located in the mesoporosity, whereas the reaction appears limited by Knudsen diffusion through zeolite micropores.

O_2-TPOs carried out on used samples showed no coke deposition suggesting a good resistance to fouling, that can be related to a very low acidity, as measured by NH_3-TPD measurements.

1. Introduction

In the field of energy transition towards more sustainable energy infrastructures and energy vectors, the conversion of methane into hydrogen and carbon dioxide by the sequence of steam reforming (eq. (1)) and water gas shift (eq. (2)) and their reverse reactions can play a significant role.

$$CH_4 + H_2O \rightleftarrows CO + 3H_2 \tag{1}$$

$$CO + H_2O \rightleftarrows CO_2 + H_2 \tag{2}$$

As a matter of fact, if biogas/biomethane is available, it can be upgraded into hydrogen by the direct steam reforming reaction and the by-produced CO_2 separated and stored/used. The so-produced hydrogen is not “green”, according to the common hydrogen colour classification, but can be defined as renewable. In the transition period, fossil natural gas can be used as raw material and, by Carbon Capture Storage/Utilization (CCS/CCU) technologies, “blue” hydrogen can be obtained. It is worth noting that the hydrogen market is expected to grow in the future due to its use in different applications, as a fuel in the transport sector and for heat production, as a chemical in several industrial productions, and as a reducing agent in metallurgy [1]. On the other hand, if the electric grid supplies excess power, electricity can be converted into hydrogen by electrolyzers and H_2 can be further converted into synthetic

---

* Corresponding author.
** Corresponding author.

E-mail addresses: gianluca.landi@cnr.it (G. Landi), serena_esposito@polito.it (S. Esposito).

https://doi.org/10.1016/j.ijhydene.2025.01.244
Received 17 July 2024; Received in revised form 12 November 2024; Accepted 14 January 2025

natural gas with CO_2 by the reverse methanation reaction, according to the Power-to-Gas strategy.

Methane steam reforming is a commercial process for hydrogen production based on several reaction units working at different operating conditions. The reformer operates at high temperatures (>800 °C) and moderate pressures (about 30 bar) and converts the natural gas and the steam into a gaseous mixture containing hydrogen, carbon monoxide, and carbon dioxide. The high temperature, required to overcome the thermodynamic constraints of the endothermic reforming reaction, precludes a full conversion of carbon monoxide into carbon dioxide, regulated by the thermodynamic equilibrium of the exothermic water gas shift (WGS) reaction. So, two WGS reactors, operating at about 300 and 200 °C respectively, follow the reformer, allowing a reduction of the CO content down to about 1 vol%. A CO_2 separation and purification stages are used to obtain a high-purity H_2 stream. Several strategies have been proposed to intensify and, possibly, simplify the reforming process, such as Membrane technology, Sorption-enhanced steam methane reforming (SE-SMR), Chemical looping steam methane reforming (CL-SMR), Chemical looping sorption-enhanced steam methane reforming (CL-SE-SMR), while Solar-assisted steam methane reforming (SA-SMR) and Electrified steam methane reforming (ES-MR) have been suggested to reduce the carbon footprint of the reforming process by using renewable energies to sustain the endothermicity of the process [2]. In this context, processes based on membrane technologies are very attractive. In a membrane reactor, hydrogen can be contextually separated during its production; thus, the thermodynamic constraints can be overcome by the continuous subtraction of a product, leading to a more favourable conversion of methane and to a higher selectivity to carbon dioxide [3]. Theoretically, the full conversion of methane and two separated high-purity streams of hydrogen and carbon dioxide can be achieved. However, the main drawback of hydrogen membranes, generally based on palladium, is related to their maximum operating temperature, not exceeding 600 °C [3]. In this context, the development of novel catalysts more active at low temperatures can pave the way for the development of effective processes based on membrane reactors.

On the other hand, as reported above, CO_2 hydrogenation emerged as a potential strategy for the storage of hydrogen in fuels with a higher volumetric power density or in fine chemicals [4–6]. Reverse water gas shift excluded, all the CO_2 hydrogenation reactions are exothermic and, thus, thermodynamically limited at high temperatures, where kinetics is generally favourable. Methanation falls in this category and, accordingly, requires low operating temperatures to achieve high CO_2/H_2 conversions and yields to methane [7].

Considering that catalysts active towards a direct reaction are generally active also towards the inverse reaction, it is not surprising that the same active phases have been proposed for both processes, i.e. steam reforming of methane and methanation of carbon dioxide. In this framework, a huge attention was devoted to nickel-based catalysts due to their low cost, good activity, and stability.

Such catalysts still appear as a suitable choice for the development of innovative SR processes due to their low cost and high activity [8–11]. Several strategies have been adopted to improve their activity and resistance to coking and sintering [8]. Several promoters were proposed, including noble metals (Pt, Ru, Rh) [12–16], coinage metals (Au, Ag, and Cu) [17–20], alkali metals (e.g., K) [21], the most active systems being those doped with noble metals. On the other hand, Ni interaction with proper support results in improved catalytic properties [22,23]. Among the supports, zeolites, such as MCM-41 [24–26] and HY [27], and mesoporous silicas [26,28,29] were proposed to enhance the catalytic performance of Ni-based reforming catalysts.

According to Ronsch et al. even if the series of activity toward the methanation reaction is Ru > Fe > Ni > Co > Mo, nickel is the most selective catalyst for methanation [30]. As stated above, the support plays a crucial role, not only in terms of its ability to disperse the active phase but also in limiting carbon deposition and CO poisoning [30]. Regarding the issue of poisoning for Ni-supported catalysts, the presence of surface acid sites can promote the formation of carbonaceous deposits on catalysts' surface with subsequent deactivation. The presence of this carbon can be limited by choosing a support with the right balance between acid-base properties or adding metal (noble and not) as promoters for Ni catalysts [2,31,32]. Furthermore, the carbon formation can be reduced by gasification with steam. This scenario introduces the need for supports with adequate resistance to pressure and temperature typical of SMR reaction.

Accordingly, several efforts have been reported to improve the catalytic performance of Ni-based catalysts towards methanation and SMR reaction through reasonable choice of support [30,33–42].

Nieva et al. [43] investigated the effect of SiO_2 and Al_2O_3 on Ni dispersion and its stability towards sintering. Applying the same incipient wetness impregnation procedure, they pointed out that the Ni mean particles size is influenced by the different surface basicity of the support. The higher density and strength of basic sites for Al_2O_3 substrate compared to SiO_2, lead to the formation of bigger Ni nanoparticles (about 20 nm and 10 nm for alumina and silica, respectively). Although the Ni particles supported on Al_2O_3 are larger, they were active and stable, while those supported on SiO_2 were unstable for the SMR reaction. Furthermore, starting from this result, they investigate the effect of a co-precipitation strategy to prepare $Ni–Al_2O_3$ catalysts, adding two metal promoters (Zn and Mg). In both cases, they achieved a higher Ni dispersion than in precipitated samples, with a relatively small size (about 6 nm). The reported results also emphasise the influence of the preparation method on catalytic activity.

The zeolites, characterized by a high surface area and well-defined porous network, appear to be good candidates as supports, for the possibility of facilitating the dispersion of Ni metallic phase, limiting their sintering [44–49]. Rossetti et al. [44] showed that a high Si/Al ratio is also decisive in the dispersion of Ni nanoparticles.

Furthermore, the acidic function of zeolites affects their catalytic activity: supports with strong acidity show low activity compared to zeolites with basic features [45,46,50]. An easy method to govern the zeolites acidity, and thus their hydrophobicity, is varying the Si/Al ratio. In this way, more hydrophobic materials would remove water from active sites more efficiently, favouring the development of the reaction [24,25,42]. The use of zeolites with a high Si/Al ratio allows also to achieve a stable catalyst considering the temperature and pressure conditions adopted during the SMR reaction [49].

In this context, we propose the use of a commercial USY zeolite with very high Si/Al ratio (>300) as support for Ni nanoparticles. The main idea is to manage acidity and to improve Ni dispersion and stability at the same time with the aim of improving both activity, durability and resistance to fouling. The amount of loaded Ni has been relatively low and varied from 5% to 20% in order to maintain a high dispersion of the active phase and reduce its load. A thorough structural, surface and textural characterization was conducted on all catalysts. The catalysts have been tested in both reactions: SMR and CO_2 hydrogenation. To the best of our knowledge, these catalysts supported onto a USY zeolite with a so high Si/Al ratio have never been proposed for SMR and CO_2 hydrogenation.

2. Materials and methods

2.1. Materials

Tosoh Corporation ultrastable Y zeolite HSZ-390HUA (Si/Al molar ratio = 385), hereafter simply named USY, was used as a base material in the preparation of catalysts. Salt nickel chloride hexahydrate (Aldrich, >98 wt %) and doubly distilled water Carlo Erba reagent grade were used in the preparation of the impregnating solution. The H_2/Ar gas mixture (H_2 3% by volume), used to create the reducing atmosphere during the thermal treatments was supplied by Nippon Gases.

For the catalytic test, CH_4, CO_2, and N_2 were obtained from high-purity cylinders (CH_4: 99.995 %; CO_2: 99.998 %; N_2: 99.9990 %;

suppliers: Air Liquid and Nippon Gases); the molecular hydrogen was produced via water electrolysis with a generator Stellargen Genius which guarantees a purity of hydrogen of 99.9999%. High-purity water was produced by a Milli-Q® EQ (7008) (Merck).

2.2. Preparation of the Ni-USY catalysts

The USY-390 zeolite (framework type FAU [51]) was subjected to the following incipient impregnation procedure under vacuum using a Carpanelli electric pump, model MM56P2, 0.15 kW, 3360 rpm. A 10 mL of double-distilled water was added to a 100 mL flask containing 1g of zeolite USY and kept under agitation for 10 min, then 15 mL of $NiCl_2{\cdot}6H_2O$ aqueous solution was added. The salt concentration was calculated to have 5, 10, and 20 % wt. nickel in the final catalyst (i.e. after heat treatment). The solution was kept under stirring for 24 h at r.t. Thereafter, the solvent was removed by evaporation at a constant temperature of 80 °C in an oven for about 24 h.

For the preparation of the catalysts, a certain amount of the Ni-impregnated zeolite was loaded in high-density Al_2O_3 vessels. Then, such vessels were put in an Al_2O_3 tubular furnace, heated (10 °C/min of heating rate) up to, 600 °C, and kept at these temperatures for 2 h under a reducing atmosphere created by a flow of a gaseous mixture Ar/H_2 (H_2 3% by volume). Then, the furnace was turned off and left to cool down to room temperature together with the materials contained therein.

From now on, we will refer to the different catalysts with the acronyms NiX, where X stands for the nominal amount of nickel, 5, 10 and 20 wt %. Ni20 catalyst after CO_2 hydrogenation reaction was labelled as Ni20_spent.

A catalyst containing 10 wt % nickel supported on γ-alumina was prepared by impregnation and used as reference. Powder γ-alumina (Sasol, South Africa) was impregnated with a proper amount of nickel nitrate hexahydrate (Sigma-Aldrich, USA) in a rotary evaporator at 55 °C, 200 mbar, and 120 rpm, dried overnight at 120 °C, and then calcined in air at 600 °C for 2 h. The sample was labelled as Ni10-A.

2.3. Materials characterization

Elemental analysis was carried out with a Rigaku NEX DE (Japan) energy dispersive X-ray fluorescence (EDXRF) spectrometer.

To test the crystallinity of the materials under investigation, preliminary XRPD patterns were collected on a Philips X'Pert diffractometer, using a Cu Kα radiation (2θ range = 5°–60°; step = 0.02° 2 θ; time per step = 100 s).

To obtain accurate quantitative phase analyses (QPA), further XPRD patterns were collected for samples Ni5, Ni10, and Ni20 in transmission mode on an θ- θ Empyrean Panalytical Diffractometer, using a Cu Kα radiation, a monochromatic I core module and PiXCel 1D detector in the angular range 7–80 with step = 0.02° 2θ; time per step = 100 s). The powders were carefully ground and loaded in the sample holder after the addition of 10 wt% of Al_2O_3, needed for amorphous quantification.

To obtain quantitative phase analyses the combined Rietveld-RIR method [52] was exploited, and the data were fitted using the EXPGUI interface [53] GSAS package [54]. For the Rietveld refinement, the starting model of the USY framework was taken from Parise et al. [55] and then refined.

The crystallite size (L) has been calculated by Scherrer formula: $L=(k\cdot\lambda)/\beta\cdot\cos\theta$, k is a constant equal to 0.90, λ is the X-ray wavelength equal to 0.154 nm, β is the full width at half maximum, and θ is the half diffraction angle. Although it is well known that Scherrer Formula cannot be used for the absolute quantification of the grain size, due to the broadening given by the instrumental function and by the strain, here we used the data as a mean of comparison among the different samples, assuming the strain being absent and the patterns collected in the same experimental conditions.

Textural properties have been evaluated through N_2 physisorption and desorption at −196 °C (ASAP2020 plus, Micrometric, USA). Before the measurement, the sample was outgassed under a high vacuum at 250 °C for 4 h to remove pollutants previously adsorbed. Due to the microporous character of zeolites, the Langmuir method was used to calculate the specific surface area but, for easy comparison with literature, BET surface area was also reported; the total pore volume (V_p) was determined from the amount of N_2 desorption at $P/P^0 = 0.98$, the micropore volume (V_{mp}) and the external surface area (S_{ext}) were determined according to the t-plot method. The evaluation of pore size distribution was obtained by the Tarazona Non-local density functional theory (NL-DFT) model [56].

The morphological characterization was performed by a field emission scanning electron microscopy (FE-SEM), ZEISS MERLIN instrument (Oberkochen, Germany) was used.

Scanning Transmission Electron Microscopy (STEM) (Bright Field) was carried out with a TALOS F200X microscope (Thermo Fisher). Concerning sample preparation, the catalyst in powder form was dispersed in isopropyl alcohol and subsequently deposited on a Cu holey carbon TEM grid by drop-casting. The analysis of STEM data was performed with the Thermo Scientific Velox software. The size distribution of Ni nanoparticles (nps) was evaluated using ImageJ software, considering almost 300 nps for each sample. Lognormal function was applied for or particle size distribution analysis.

The experimental setup used to conduct H_2-TPR and O_2-TPO experiments was described elsewhere [57], i.e. in the same experimental setup used for catalytic tests (see Section 2.4). The catalyst (0.5 g) was placed in a quartz reactor. The gas flow rate (2 vol% H_2/N_2 and 2 vol% O_2/N_2 for H_2-TPR and O_2-TPO, respectively) was set at 10 l(STP)/h. The temperature was increased from room temperature up to 600 °C (heating rate: 10 °C/min; time at 600 °C: 20 min) by an electric furnace. H_2-TPR experiments were carried out before catalytic tests, while O_2-TPD experiments were performed at the end of the experimental campaign regarding the catalytic activity [58].

TPD was carried out by using a Micromeritics TPD/TPR 2900 analyser (USA), equipped with a thermal conductivity detector; a 2 vol% NH_3/He mixture at a flow rate of 0,055 mL/min (55 cm^3/min) was flowed through the samples for 30 min at ambient temperature to fully adsorb the NH_3 on the acid sites; then samples underwent a 0.05 mL/min He flow and a heating rate of 10 °C/min from room temperature up to 600 °C. Samples were not pre-treated.

2.4. Catalytic tests

The powdered catalysts (0.5 g) were tested in the experimental setup described elsewhere [59,60] and described in Section S.1(see Fig. SI1) without any pretreatment. Catalytic tests were conducted at a constant contact time, defined as the ratio of catalyst weight to flow rate, set at 0.09 g s cm^{-3}. The reaction temperature ranged from 450 to 600 °C.

Two distinct sets of measurements were carried out. For methane steam reforming, the feed was composed of CH_4 (3 vol%) and H_2O (6 vol %) in N_2. For the CO_2 hydrogenation, the feed was composed of CO_2 (3 vol%) and H_2 (12 vol%) in N_2. Very dilute reaction mixtures reduce the thermal effects related to thermality of the reactions and thus provide experimental results under pseudo-isothermal conditions.

CH_4 conversion for the steam reforming reaction was evaluated as:

$$x_{CH_4} = \frac{CH_4^{IN} - CH_4^{OUT}}{CH_4^{IN}}$$

H_2 yield was defined as:

$$Y_{H_2} = \frac{H_2^{OUT}}{4\cdot CH_4^{IN}}\cdot 100$$

CO_2 conversion in the hydrogenation reaction was determined using the following equation:

$$x_{CO_2} = \frac{CO_2^{IN} - CO_2^{OUT}}{CO_2^{IN}}$$

while the selectivity to CH_4 and CO were defined as:

$$s_{CH_4} = \frac{CH_4^{OUT} - CH_4^{IN}}{CO_2^{IN} - CO_2^{OUT}}$$

$$s_{CO} = \frac{CO^{OUT} - CO^{IN}}{CO_2^{IN} - CO_2^{OUT}}$$

Equilibrium calculations were carried out using Aspen Plus (AspenTech) by considering an isothermal RGIBBS reactor. Once the operating conditions were specified, the results were determined on the basis of the minimization of Gibbs free energy.

Furthermore, it is required to verify the presence of resistance to internal diffusive transport and, in agreement with Satterfield and Sherwood [61], it is known that pore diffusion may occur by ordinary and Knudsen diffusion. The ordinary diffusion of methane in nitrogen is estimated by the following equation:

$$D_M = 1.858\cdot 10^{-3}\cdot T^{1.5}\cdot \frac{\sqrt{\frac{M_{CH4}+M_{N_2}}{M_{CH4}\cdot M_{N_2}}}}{P\cdot \sigma^2_{CH4-N_2}\cdot \Omega_D}$$

Where D_M is the molecular or ordinary diffusivity ($cm^2\cdot s^{-1}$), M is the molecular weight ($g\cdot mol^{-1}$), T is the temperature (K), P is the total pressure (atm), σ^2 is the first Lennard-Jones parameter (Å), Ω_D is an adimensional function of temperature and intermolecular potential of the binary gas mixture.

It can be inferred that the D_M is a function of pressure (i.e. constant flux with pressure) and is independent on pore size while Knudsen diffusivity is independent on pressure and dependent on pore size according to the formula:

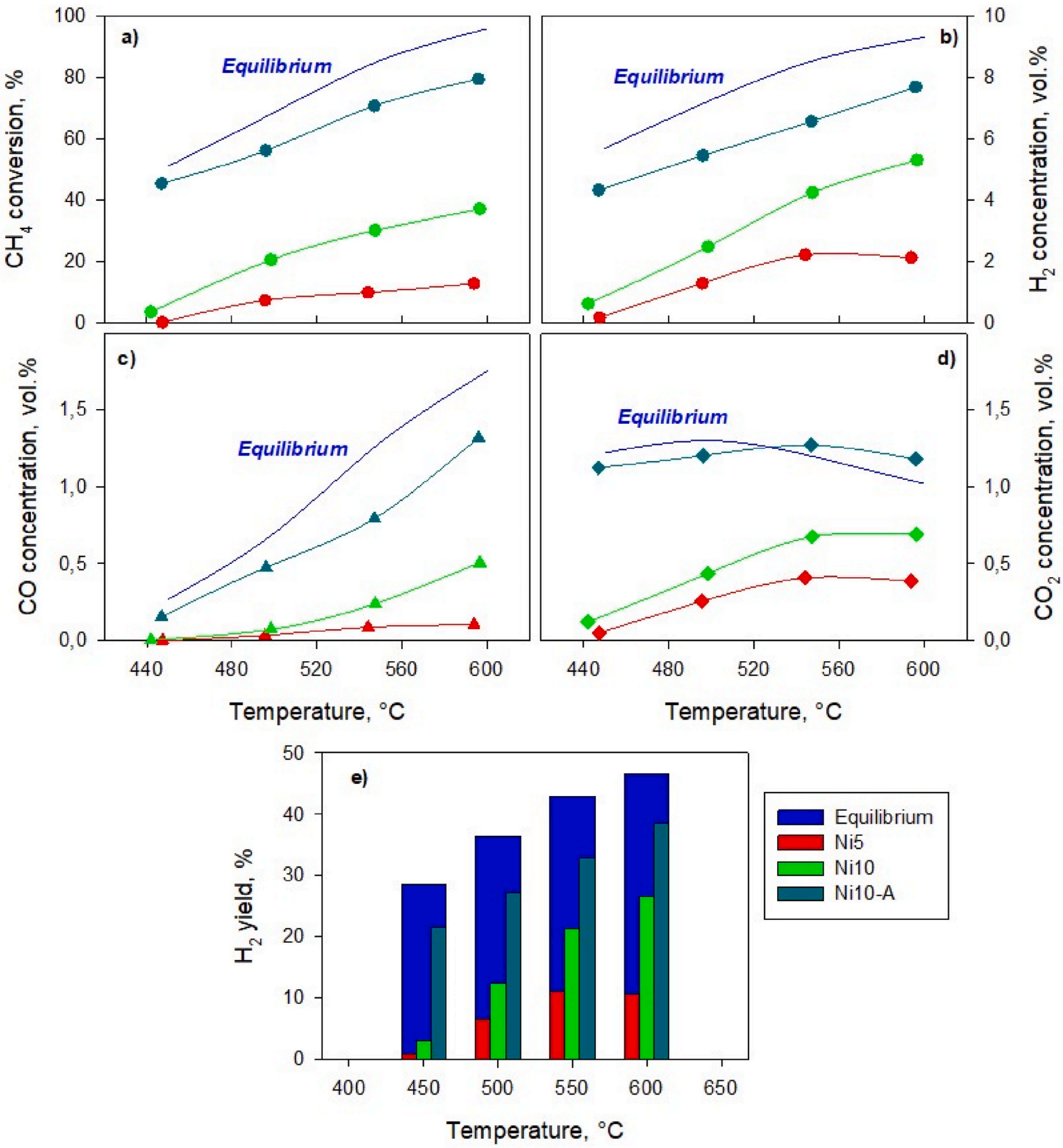

Fig. 1. CH_4 conversion (a), product distribution (b: H_2; c: CO; d: CO_2), and H_2 yield (e) as a function of temperature of Ni5 (red lines/bars), Ni10 (green lines/bars), and Ni10-A (cyan lines/bars) catalysts. Blue continuous curves/bars represent the equilibrium values. (For interpretation of the references to colour in this figure legend, the reader is referred to the Web version of this article.)

$$D_K = \frac{d}{3} \cdot \sqrt{\frac{8 \cdot R \cdot T}{\pi \cdot M_{CH4}}}$$

where D_K is the Knudsen diffusivity ($m^2 \cdot s^{-1}$), d is the pore diameter (m), T is the temperature (K), M is the molecular weight of the diffusing species, e.g. methane ($g \cdot mol^{-1}$), R is the ideal gas constant ($J \cdot K^{-1} \cdot mol^{-1}$).

The overall net diffusivity D was evaluated as a weighted average between D_M and D_K, according to the expression:

$$D = \left(\frac{1}{D_M} + \frac{1}{D_k} \right)^{-1}$$

while the effective diffusion is estimated by the following equation:

$$D_{eff} = \frac{\varepsilon}{\tau} \cdot D$$

where D_{eff} is the effective diffusion in pores (cm^2/s), ε and τ are the void and the tortuosity factors respectively.

The impact of intraphase transport limitation is considered according to the Weisz-Prater criterion [62]:

$$\Phi = \frac{d_p{}^2 \cdot r}{4 \cdot D_{eff} \cdot C_s} < 0.3$$

Where Φ is the Weisz modulus (adimensional), d_p is the catalyst particle diameter (cm), r is the volumetric reaction rate ($mol \cdot s^{-1} \cdot cm^{-3}$), C_s is the external surface concentration of reactant ($mol \cdot cm^{-3}$).

3. Results and discussion

3.1. Steam methane reforming reaction

Reaction tests conducted on Ni20 showed that this catalyst is not active for the SMR reaction. On the other hand, samples with lower Ni loading (Ni5 and Ni10) showed a non-negligible catalytic activity (Fig. 1). Specifically, the Ni10 exhibited higher CH_4 conversions compared to the Ni5, but both displayed a qualitatively similar trend (see Fig. 1a). Fig. 1(b–d) shows the product distribution in terms of volumetric percentage on a dry basis displayed by analysis system, while Fig. 1e shows H_2 yield. CO_2 is the main carbon-containing product with selectivity ranging from about 60% (on Ni10 at 600 °C) to about 98% (on both samples at 450 °C), suggesting a good activity towards water gas shift reaction. The WGS activity also increases hydrogen productivity, as evidenced in Fig. 1b, especially on the most active catalyst (i.e. Ni10). Reference catalyst showed higher activity than USY samples towards both methane activation, as suggested by the higher conversions (Fig. 1a), and WGS, as suggested by the CO_2 partial pressure approaching the thermodynamic value (Fig. 1d).

Methane conversion in the steam reforming reaction is far enough from thermodynamic equilibrium to consider the reverse reaction negligible. Thus, conversion from 500 to 600 °C can be fitted with a pseudo-first order kinetics and the corresponding activation energies and frequency factors can be calculated. Fig. 2 shows the Arrhenius plot for both catalysts, while Table 1 reports the kinetic parameters. As shown in Table 1, increasing the active phase increases the frequency factor. Activation energies are low with respect to values reported in the literature, ranging around 100 kJ mol^{-1} [63], suggesting a significant role of transport phenomena. As reported in Section 2.4, the Weisz-Prater criterion has been used to determine the importance of internal diffusion using all observable variables. Properly in the case of integral reactor, the C_s (concentration on the external particle surface) should be replaced by the proper average of the varying concentrations. However, in the case of this preliminary study, it is enough to estimate the Weisz modulus for the initial CH_4 concentration. Table 2 shows the calculated diffusivities and the corresponding Weisz modulus for Ni5 and Ni10 samples. It is worth noting that the negligibility of the reverse reaction cannot be assumed on Ni10-A sample, showing performance not far from the thermodynamic equilibrium. Accordingly, the relative kinetics parameters cannot be calculated by the procedure used for NiX samples.

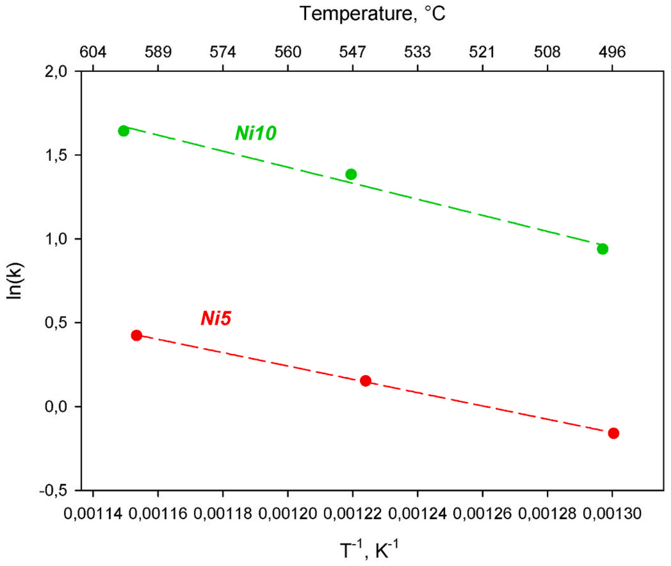

Fig. 2. Arrhenius plot for SMR on Ni5 and Ni10.

Table 1
Frequency factor (k_0, $cm^3\ g^{-1}\ s^{-1}$), Turnover frequency for hydrogen production (TOF with respect total Ni (s^{-1}); TOF_s with respect to Ni surface, $mol_{H2}\ m^{-2}\ s^{-1}$), and activation energy (E_a, kJ mol^{-1}) calculated for 5 Ni and 10 Ni.

Sample	Ni5	Ni10
k_0	5.01 ± 0.10	7.17 ± 0.73
TOF	880 ± 17	630 ± 64
TOF_s	2.11 ± 0.04	2.65 ± 0.26
E_a	33.0 ± 0.7	39.8 ± 4.9

Table 2
Methane diffusivities ($m^2 \cdot s^{-1}$) and Φ values calculated for 5 Ni and 10 Ni. Methane steam reforming reaction tests.

Sample	T (°C)	D_M	D_k	D	D_{eff}	Φ
Ni5	496	1.11	$2.96 \cdot 10^{-3}$	$2.95 \cdot 10^{-3}$	$2.21 \cdot 10^{-4}$	0.43
	544	1.23	$3.05 \cdot 10^{-3}$	$3.04 \cdot 10^{-3}$	$2.28 \cdot 10^{-4}$	0.58
	594	1.36	$3.14 \cdot 10^{-3}$	$3.13 \cdot 10^{-3}$	$2.35 \cdot 10^{-4}$	0.73
Ni10	498	1.12	$2.96 \cdot 10^{-3}$	$2.95 \cdot 10^{-3}$	$2.21 \cdot 10^{-4}$	0.90
	547	1.24	$3.05 \cdot 10^{-3}$	$3.05 \cdot 10^{-3}$	$2.28 \cdot 10^{-4}$	1.37
	597	1.37	$3.14 \cdot 10^{-3}$	$3.14 \cdot 10^{-3}$	$2.35 \cdot 10^{-4}$	1.72

$\varepsilon = 0.3$; $\tau = 4$.

All the tests were performed over the same sample which worked for more than 50 h. At the end of the whole experimental campaign, catalytic tests were repeated to verify the catalyst stability. The results (not reported) were within the experimental error (±5%), suggesting good stability of NiX catalysts.

As shown in Table 2, the Knudsen diffusivity is significantly lower than the ordinary one (about 300 times higher); so, D is, with good approximation, equal to the Knudsen diffusivity, whose mechanism regulates diffusion of reactants and products. The estimated Φ values for methane steam reforming are always greater than 0.3 and, as expected, increase by increasing the temperature and the nickel content. Therefore, the reaction is affected by internal diffusive transport.

Concerning performance reported in the literature, it is worth noting that zeolites have been proposed as supports in the case of dry reforming rather than steam reforming [24–27]. This could be due to the dealumination phenomena of zeolites occurring at high steam partial pressures and temperatures typical of the reforming processes [64]. On the contrary, the very high Si/Al ratio of our catalysts guarantees high resistance to dealumination, making these samples suitable for methane steam reforming. Moreover, the negligible acidity of the working samples, *vide infra*, provides a very low methane decomposition rate and, thus, a good resistance to fouling. In terms of activity, catalysts providing better performance are generally characterized by higher metal loadings and/or more complex formulations and/or more complex preparation methods [65–69] than those proposed in this work, characterized by a low Ni content (<10 wt%), a simple composition (no dopant; commercial support), and a simple preparation method (wet impregnation). However, a full economic analysis is beyond the scope of this work.

3.2. CO_2 hydrogenation

Fig. 3 shows the CO_2 conversion and the selectivity to CH_4 as a function of the reaction temperature. The 20Ni sample, which is inactive towards the SMR reaction, exhibits good activity in the CO_2 hydrogenation. Furthermore, the curve of experimental points is qualitatively similar to the thermodynamic equilibrium curve, inclusive of the methanation reaction, as opposed to the thermodynamic equilibrium curve restricted to only the Reverse Water Gas Shift (RWGS) reaction. In contrast, the Ni5 and Ni10 catalysts, which were active in the SMR reaction, show a trend of the experimental points resembling the qualitative trend of the restricted thermodynamic equilibrium curve for CO_2 hydrogenation. This agrees with the selectivity towards the different products (Fig. 3). As a matter of fact, Ni5 and Ni10 show a negligible selectivity to methane, thus resulting to be selectively active towards RWGS. On the contrary, the Ni20 sample appears to be more selective towards CH_4 and less selective towards CO. The reference sample supported on γ-alumina is active towards methanation, showing catalytic performance approching the thermodynamic equilibrium in the whole temperature range.

The experimental curve of CO_2 conversion as a function of reaction temperature (450–600 °C) for the Ni20 sample employed in this work shows a similar trend of its thermodynamic equilibrium curve with a maximum value of conversion of about 40% with GHSV = 12000 h^{-1} and a high selectivity to methane. Comparing this sample to other Ni-based methanation catalysts is not straightforward due to the different temperature ranges and contact times. For instance, Guo et al. reported that Ni/ZSM-5 catalyst exhibits a maximum CO_2 conversion of about 76% at 400 °C and at GHSV = 2400 h^{-1} [70], i.e. at a contact time 6 times higher than that adopted in this work. Similarly, Ni-modified 13X and 5A zeolite catalysts were tested by Wei et al. [44], showing CO_2 conversion close to the thermodynamic equilibrium starting from 360 °C at GHSV = 13333 mL g^{-1} h^{-1} (corresponding to 0.54 g s cm^{-3}; 6 times higher than that adopted in this work). On the other hand, better performance was reported by Sholeha et al. on a 15 wt% Ni/NaY catalyst, reaching 75% CO_2 conversion (close to the thermodynamic equilibrium) at 450 °C and at GHSV = 50 000 mL g^{-1} h^{-1}, corresponding to 0.072 g s cm^{-3} [45]. It is worth noting that the mass transfer limitations detected for methane reforming can affect the hydrogenation performance of our catalysts too.

With respect to the reverse water gas shift reaction, the good dispersion of nickel on Ni5 and Ni10, leading to small nanoparticles (see Section 2.3), allows our samples to perform better than 7 wt% Ni supported on nanocrystalline MgO [71]. On the other hand, Ni nanoparticles supported on N-doped silica [72] show higher intrinsic activity towards RWGS, probably due to their larger pores, improving intraparticle mass transfer, while the good activity of bimetallic Cu–Ni nanoalloys supported on alumina [73] can be addressed to the modified electronic properties of the bimetallic alloys with respect to monometallic nickel.

3.3. Structural, surface, and textural characterization

In the present work, an ultra-stable zeolite, USY-390, purchased from the Tosoh corporation, was used as a nickel metal support. Such zeolite is characterized by a markedly high silicon/aluminium molar ratio (Si/Al = 385), where the extra-lattice cation is hydrogen, while the only detectable metal cation (Na^+) is present in very small quantities, Table 3. Due to its reduced cation exchange capacity, it was subjected to an impregnation treatment with an aqueous solution of nickel chloride hexahydrate, $NiCl_2{\cdot}6H_2O$. The nickel ions within the zeolitic structure give the material a teal colour (typical of nickel (II) aqueous complexes, $[Ni(H_2O)_6^{2+}]$, that turns black after reduction treatment at 600 °C, suggesting the formation of metallic nickel, Fig. SI2. Before describing the features of the obtained catalysts, some words justifying their preparation procedure appear necessary, as an uncommon precursor ($NiCl_2{\cdot}6H_2O$) and a reduction temperature of (600 °C) were selected.

Table 3
Physico-chemical data of USY zeolite provided by Tosoh Corporation.

Zeolite USY-390	HSZ-390HUA
Cation type	H
SiO_2/Al_2O_3	770
Na_2O	0.01 wt. %
Crystal system	Cubic
Unit cell size	24.27 Å
Grain size	5.00–7.00 μm
Specific surface area (BET)	630 m^2/g
NH_3-TPD	0.1 mmol/g

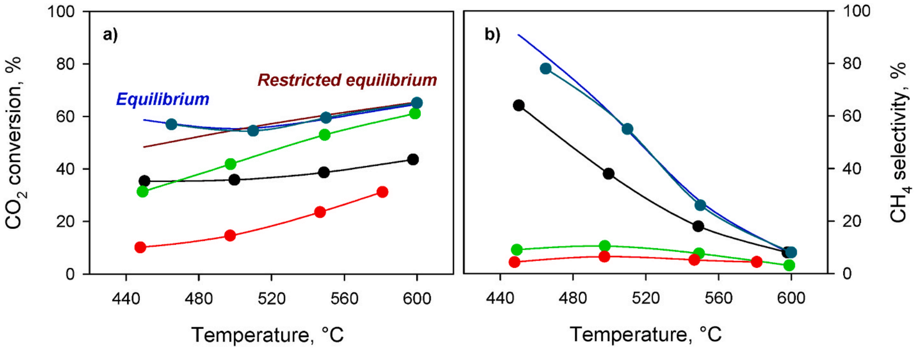

Fig. 3. CO_2 conversion (a), CH_4 selectivity (b) as a function of temperature of Ni5 (red lines), Ni10 (green curves), Ni20 (black curves), and Ni10-A (cyan lines) catalysts. Blue continuous curve represents the complete equilibrium conversion, brown continuous curve represents the restricted equilibrium conversion. (For interpretation of the references to colour in this figure legend, the reader is referred to the Web version of this article.)

Both these choices went into the direction of maximizing the metallic Ni amount in the final catalysts. Unlike the nitrate salt, $NiCl_2{\cdot}6H_2O$ does not result in the production of O_2 (which could make less reducing the environment) during the thermal treatment. In turn, the high reduction temperature selected (600 °C) was necessary on account of $NiCl_2{\cdot}6H_2O$ higher stability than the nitrate salt and to ensure a complete reduction of Ni. As evidenced by the TPR results, *vide infra*, the adopted heat treatment was effective for a complete reduction of the nickel loaded in the zeolite. The chemical composition of the elements in the NiX samples, obtained by XRF analysis, indicates a good correspondence with the nominal values. In particular, the Ni weight percentage in the Ni5, Ni10 and Ni20 catalysts is 4.5, 7.8 and 23 %, respectively. Moreover, the Si/Al ratios of fresh and used samples are in good agreement with the nominal one, suggesting that no dealumination occurs during both the preparation and the reaction.

Fig. 4 reports the preliminary X-ray diffraction (XRD) patterns of the pristine USY zeolite and NiX catalysts. The USY zeolite shows diffraction peaks characteristic of a strongly dealuminated Y zeolite (JCPDS card no. 81–2467), and these are preserved in Ni-containing samples, suggesting that the preparation procedure preserves the zeolite structure.

The sharp peak at about 44° 2θ in the pattern of NiX catalysts is ascribed to the most intense diffraction plane (111) of Ni^0 (JCPDS card no: 87–712). As the comparison of XRD patterns clearly shows, the intensity of this peak rises with increasing nickel content, reaching a maximum for sample Ni20. The size of nickel crystallite has been calculated by applying the Scherrer formula to the most relevant peaks. The amount of nickel influences the size of metal crystallites, which increases from about 32 nm for Ni5 to about 45 nm for Ni20 (for more detail about peak position and calculation see Table SI1). X-ray diffraction pattern was obtained for the Ni20_spent sample, Fig. SI3, showing a small increase in the relative intensity of the peaks associated with the Ni^0. The size of the metallic crystallites, 50 nm, is only slightly larger than the initial value of 45 nm obtained for Ni20.

The QPA (quantitative phase analyses) obtained by high-resolution diffraction pattern reported in Table 4 clearly indicate the increase of metallic Ni content with increasing the Ni loading of the starting impregnation batch. The results are quite consistent with the data of the chemical analyses, considering that diffraction patterns are collected on a very small amount of sample. The amount of zeolite and of amorphous phase seems to decrease in the highest Ni sample, but this is only the effect of the increase of metallic Ni. The calculated and observed patterns are in Figures SI4, SI.5, SI.6 of supplementary materials.

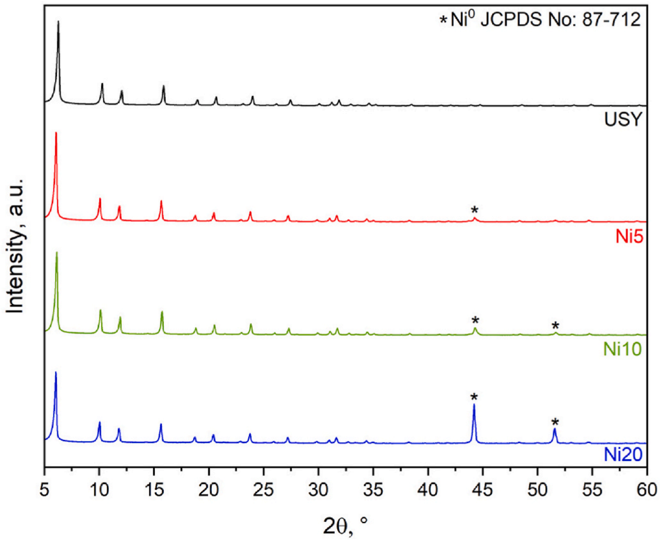

Fig. 4. XRD pattern of pristine zeolite (USY) and Ni-based catalysts.

Table 4
Results of QPA (quantitative phase analyses) and goodness of fit parameters (χ^2, Rwp, R(F^2) are goodness of fit parameter as expressed by GSAS software).

%wt	Ni5	Ni10	Ni20
USY	59.1	55.0	46.7
Metallic Ni	5.9	9.4	28.3
Amorphous phase	35.0	35.5	25.1
χ^2	2.884	3.755	3.243
Rwp	16.2	15.9	14.4
R(F^2)	11.3	11.9	11.9

The degree of nickel reduction in the catalysts was verified by H_2-TPR analysis, in which no hydrogen consumption was detected (see Supporting Materials, Fig. SI7). This confirms that nickel is exclusively present as Ni^0. The textural properties were assessed by N_2 physisorption measurements. The adsorption/desorption isotherms of USY and heat-treated samples, Ni5, Ni10, and Ni20, are shown in Fig. 5a. The isotherms of all the samples can be described as a combination of type I, characterised by a steep rise in N_2 adsorption at very low relative pressures, representative of micropore filling, and type II, characterised by an increasing slope at p/p^0 greater than 0.4. The presence of an H4-type hysteresis loop suggests the presence of large mesopores/macropores likely to be generated by the dealumination treatment of zeolite Y [74,75].

A thorough porosity evaluation was performed using an NL-DFT model, Fig. 5b. The main peak in the pore size distribution is centred on the mean value of 8.8 Å distinctive for this specific zeolite, with a minor contribution in the range of 12–15 Å due to the presence of small mesopores [76]. The presence of a fraction of large porosities, above 40 nm, can be deduced when representing the porous volume using a cumulative curve, Figure SI8.

The parameters obtained by processing the adsorption/desorption isotherms are shown in Table 5. Given the presence of mixed porosity, although the zeolites are predominantly microporous, we have reported both Langmuir and BET-specific surface areas. Both models show a detrimental effect of nickel leading to a gradual decrease in the specific surface area. This effect could be caused by a partial plugging of the pores, which would also contribute to a decrease in pore volume, with a more relevant effect on that generated by mesopores [77]. However, the Ni20 sample still possesses a significant surface area compared to different zeolite-supported nickel catalysts reported in literature [34, 35].

While a high surface area is a factor that has a notable impact on the dispersion of nickel particles, mesoporosity is reported to play an important role in catalyst stability and the reduction of carbon coke [34]. In further support of the finding that we are not dealing with an exclusively microporous zeolite with a typical type I isotherm, there is the presence of an appreciable external surface area which adds its effect to that of the micropores (Table 5). The trend of the external surface values follows that of the specific surface area, being greater in pristine zeolite [37,78].

Scanning electron microscopy measurement (SEM) was conducted to evaluate the morphology of the zeolite–supported nickel catalysts. The SEM images (Fig. 6) show, for all catalysts, the typical structure of ultrastable Y zeolite [79] is preserved with the presence of disordered crystals (100–300 nm) that are prone to form agglomerates. The morphology of Ni-USY samples does not change significantly as a consequence of both heat treatment and nickel amount, indicating that the zeolite support is almost stable during the catalyst's preparation [42, 80].

The STEM micrographs and mapping data, reported in Fig. 7, showed the presence of dense globular shaped particles, attributed to Ni by EDS maps [81]. The metallic Ni nanoparticles, confirmed by XRD, are dispersed on the preserved zeolite crystals [82]. Ni5 and Ni10 catalysts show size distributions of the Ni-NPs centred at 15 and 50 nm, respectively (as reported in the red and green histogram Fig. 7). For the Ni20 sample, the dense material is still uniformly distributed but has a larger

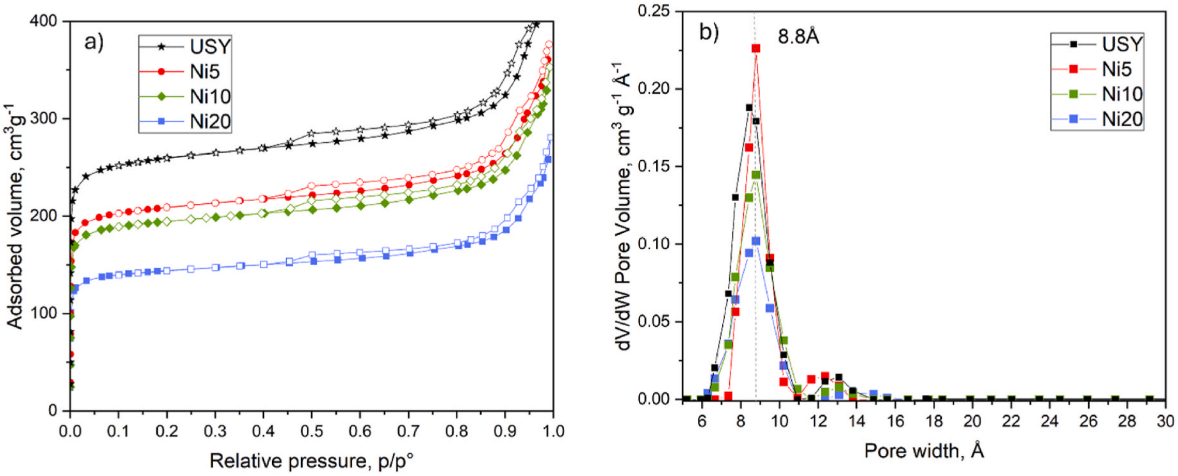

Fig. 5. a) N_2 adsorption/desorption isotherms at −196 °C of USY, Ni5, Ni10 and Ni20. Adsorption and desorption branches were indicated with filled and empty symbols, respectively; b) Pore size distribution was obtained by applying the Tarazona NLDFT method.

Table 5
Textural and crystallographic data of the USY zeolite and Ni-based catalysts.

Sample				t-plot			
		$S_{Langmuir}$ (m^2g^{-1})	S^a_{BET} (m^2g^{-1})	S^b_{ext} (m^2g^{-1})	V_{mp} (cm^3g^{-1})	V_{meso} (cm^3g^{-1})	V_p (cm^3g^{-1})
USY		1166	750	165	0.30	0.37	0.67
Ni5		913	628	136	0.26	0.29	0.55
Ni10	850	584	132	0.24	0.27	0.51	
Ni20	638	438	120	0.17	0.23	0.40	

[a] Range 0.20-0.3 P/P0, C_{BET} negative.
[b] Sext range 0.3–0.4 nm thickness.

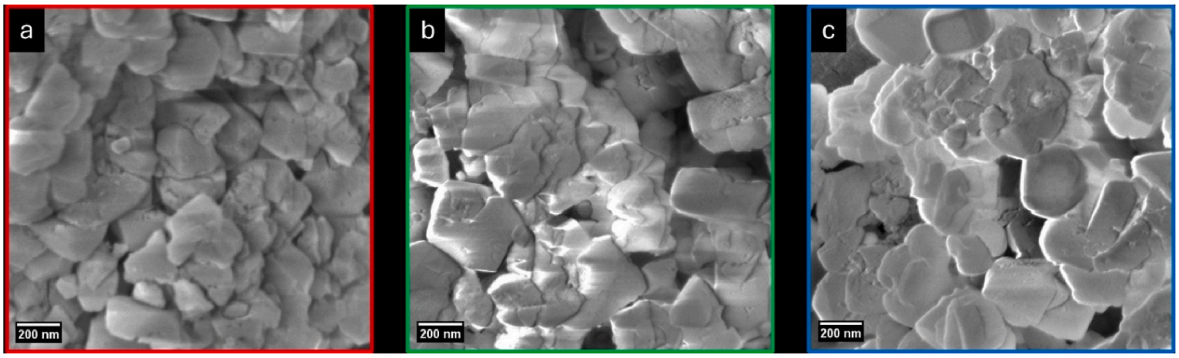

Fig. 6. Selected SEM images of a) Ni5, b) Ni10 and c) Ni20.

size, with the size distribution of Ni-NPs centred around a value of 180 nm (Fig. 7, blue histogram). Nevertheless, the size distribution is retained in Ni20_spent sample, Fig. SI9, showing stability toward CO_2 hydrogenation reaction, in agreement with XRD diffraction.

Specific surface areas of metal nanoparticles have been calculated according to the following equation [83]:

$$NiSSA = \frac{3\sum n_i r_i^2}{\rho_{Ni}\sum n_i r_i^3}$$

where r_i is the mean radius of the size class containing n_i particles, and ρ_{Ni} is the volumetric mass of Ni (8.91 g cm^{-3}). NiSSA of Ni5, Ni10, and Ni20 are 6.5, 4.2, and 1.5 m^2 g^{-1} respectively. The comparison of the size distribution of the obtained metallic Ni particles with literature data does not appear straightforward as the reported literature [44–49] usually claims the occurrence of NiO particles. The coalescence phenomena of metallic Ni particles are other than those of NiO particles.

At high magnification, Fig. 8, is possible to distinguish the presence of surface cavity, mainly due to the leaching procedure for obtaining the dealuminated zeolite [84] and of intra-crystal mesopores [75]. The presence of these secondary pores (in addition to the micropore structure that has been preserved in all thermally treated samples) allows us to define a hierarchical architecture for the prepared catalyst. Indeed, in a typical hierarchical catalyst, different pores systems (micro- and meso/macro-) are interconnected [85,86]. This feature emerges as an advantage over the reactions under study because it reduces the diffusion problems typical of microporous zeolites and improve the exposure of multiple active sites. Hierarchical zeolite-based catalysts are promising in various catalytic reactions [87].

About the Ni20 sample, the formation of large particles, as evidenced by TEM, is responsible for its inactivity towards SMR (Section 3.1). As a

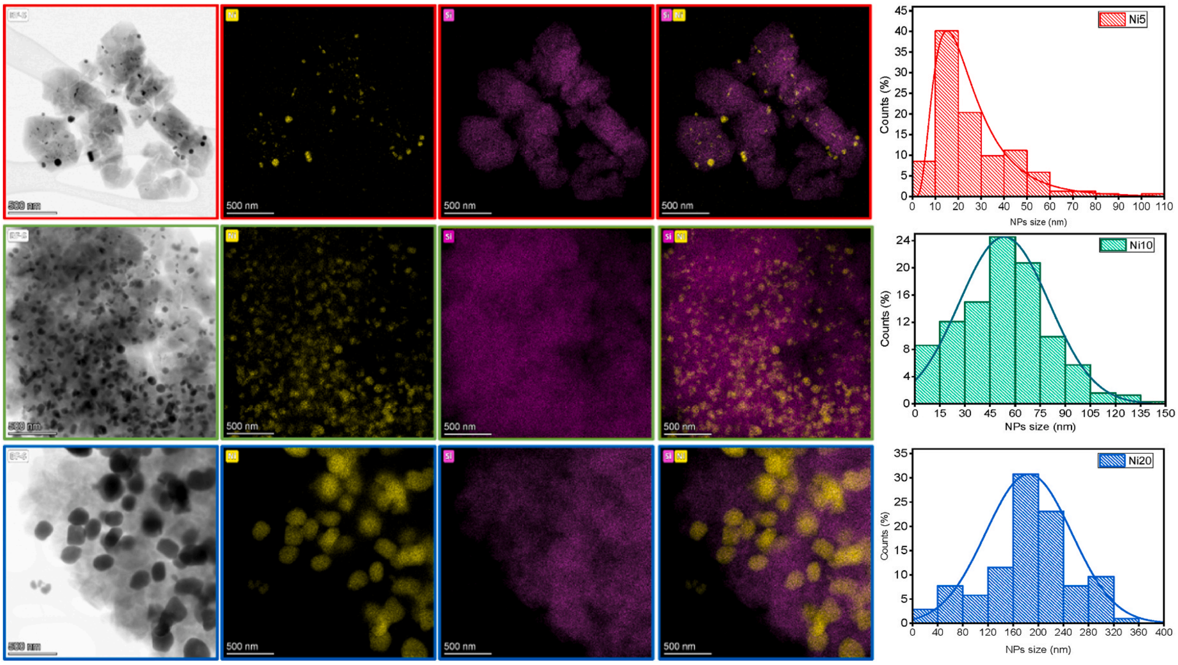

Fig. 7. Selected STEM micrographs with relative EDS map, from top to bottom: Ni5, Ni10 and Ni20. Colour code for element: Ni yellow and Si purple. (For interpretation of the references to colour in this figure legend, the reader is referred to the Web version of this article.)

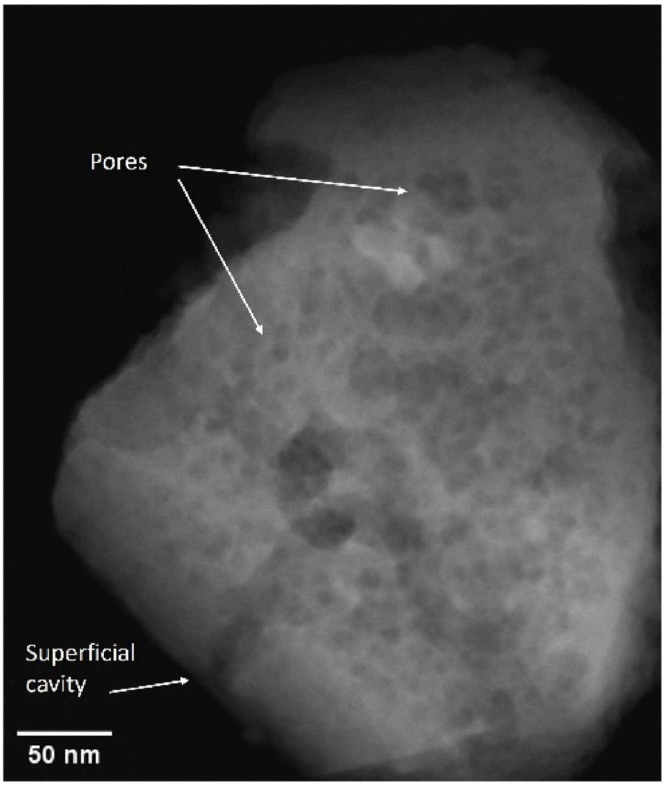

Fig. 8. STEM micrograph (detector High Angle Annular Dark Field, HAADF) of the dealuminated USY zeolite taken at high magnification.

matter of fact, SMR activity shows a structure sensitivity, as highlighted with Ni nanoparticles supported on SiO_2, which exhibited a decreasing activity with increasing nanoparticle size [88]. On the other hand, with regards to Ni5 and Ni10, as shown in Table 1, increasing the active phase by 1.76 times (according to XRF analysis) corresponds to 1.5 times increase in the frequency factor. Because the frequency factor can be considered directly proportional to the number of active sites, this result suggests that a part of the added nickel is hindered, in agreement with the TEM results, highlighting the larger size of Ni particles. As a matter of fact, TOF_s (Table 1) are quite similar, suggesting that the exposed Ni surface is the key parameter for methane activation.

The different particle size distributions can also explain the different activity of the samples towards CO_2 hydrogenation (Section 3.2). As a matter of fact, the different activity towards methanation and RWGS is related to the structure-activity relationship [89]. In particular, large Ni nanoparticles are active towards CH_4 production, while small Ni nanoparticles can activate only RWGS.

Moreover, the above results show the significance of the accessibility of active sites. As reported in Sections 3.1 and 3.2, the small pores of USY (8.8 Å) represent a resistance for mass transfer from the outer surface of the catalyst particle to the particle core. However, TEM analysis with the evaluation of the particle size distribution suggests that Ni nanoparticles cannot be hosted within so small pores, but within the mesoporosity detected by N_2 physisorption. Accordingly, reactants (products) must diffuse (counter diffuse) through the small USY pores to access to Ni nanoparticle before (after) the catalysed reaction occurs. Pros and cons of hierarchical catalytic systems have been previously reported [85–87, 90–93]; in particular, it has been reported that hierarchical structure can affect mass (and heat) transfer [94] and metal dispersion on the support [95], both affecting the catalytic performance.

It is worth noting that mass transfer limitations and structure sensitiveness are not generally detected at the same time, the latter commonly occurring under kinetic regime. Peculiarly, Ni-USY catalysts show a coexistence of internal mass transfer limitations and structure sensitiveness. As reported in Refs. [88,89], the catalytic activity strongly depends on the Ni particle size. In our case, a threshold behaviour can be identified; smaller particles in Ni5 and Ni10 are active towards SMR and RWGS, but fully inactive towards methanation, while large particles in Ni20 are active towards methanation, but fully inactive towards SMR. Accordingly, no conversion towards “inactive” reactions can be detected independently from the mass transfer rate; on the contrary, the catalysts are active enough to detect mass transfer limitation when “active” reactions are performed.

3.4. *Temperature programmed analyses (NH_3-TPD, TPO)*

NH_3-TPD profiles of fresh and used catalysts are reported in Fig. 9. All the samples are characterized by an evident disparity. Fresh samples are characterized by an intense low-temperature peak (at 75 °C) and a wide desorption at medium-high temperatures (at 390 °C, 435 °C, and 570 °C). Under reaction conditions, a significant suppression of the acidity occurs, especially at medium-high temperatures, while the low-temperature peak experiences a decrease but remains quantifiable.

Comparison with literature findings makes it clear that the medium temperature peaks are linked to Brønsted and Lewis acidic sites, while adsorption on Si–OH groups gives rise to the low-temperature peak [74]. Despite the different Si/Al ratio of an order of magnitude [74], the comparable qualitative behaviour suggests that the proposed peak assignment is consistent. Table 6 shows the quantitative analysis of NH_3-TPD experiments, underlining the impact of the reaction conditions on acidity. The number of acid sites is reduced by about one order of magnitude; the overall acidity decreases by increasing the Ni content on used samples, while a non-linear behaviour is detected on fresh samples. Figure SI10 and Table 6 suggest that, excluding weak sites detected as “peak 1” being quite constant, a transformation of acid sites occurs by increasing the Ni content on fresh samples. In particular, the number of acid sites of Ni5 steadily decreases as acidity strength increases, while on Ni10 the number of medium-strength sites significantly increases and an increase is detected on strong acid sites too, suggesting an increase of the strength of the acid sites by increasing the Ni content. On the contrary, a further increase of the Ni loading induces a full conversion of the medium and strong acid sites into weak ones.

With respect to other Y zeolites, similar overall amounts of acid sites were reported in Refs. [49,84] on samples with lower Si/Al ratios (25–30), while larger NH_3 desorption (about 2 mmol/g) was detected by Silva et al. [96] on a H–Y zeolite.

As reported in Section 2.3, after several reaction tests both hydrogenation CO_2 and steam reforming reactions (corresponding to about 50 h under reaction conditions), a TPO was carried out to evaluate the carbon formation on the used catalysts. Under the selected reaction conditions, no coke formation is thermodynamically predicted. However, coke can be formed (and not consumed) due to kinetic reasons [43]. Fig. 10 shows O_2 consumption and CO_2 production in the NiX samples. CO_2 production on Ni5 and Ni10 is negligible, while a detectable CO_2 concentration is measured during TPO on Ni20. Two peaks are detected at about 450 and 600 °C attributable to amorphous and filamentous carbon respectively [97]. Even on this sample, the coke selectivity, estimated to be around 10^{-4} (mole of coke produced per mole of reacted carbon in methane and/or CO_2) with a production rate of $5.6 \bullet 10^{-5}$ (mole of coke produced per mole of reacted carbon in methane and/or CO_2 per second), shows an exceptionally low value, suggesting a good resistance of USY-supported Ni catalysts towards fouling, positively affecting catalyst efficiency and lifespan. On the other hand, a similar resistance to coking has not been detected on Ni10-A, showing a coke selectivity around $9.8 \bullet 10^{-4}$ (mole of coke produced per mole of reacted carbon in methane and/or CO_2) with a production rate of $5.5 \bullet 10^{-4}$ (mole of coke produced per mole of reacted carbon in methane and/or CO_2 per second). The significant consumption of oxygen shown in Fig. 10 can be mainly attributed to the Ni oxidation.

Noteworthy is the observation that the low coke formation can be attributed to the low acidity of the sample (see Section 3.3), enhanced by its reduction under reaction conditions. The low selectivity to carbon black is predominantly associated with the catalyst’s minimal acidity [98]. The reduction and reforming reactions are primarily activated by the redox properties of nickel, while acidity contributes to carbon black formation in the reforming process [99]; accordingly, the addition of basic elements improves coke resistance [100,101]. Other key points could be related to the dimension of the Ni nanoparticles, affecting methane decomposition by modifying the carbon growth rate [102], and the pore structure of the zeolite, affecting the carbon deposition rate by modifying the accessibility to the active sites [103].

4. Conclusions

Ni nanoparticles supported on commercial USY zeolites were prepared, characterized, and tested towards two reactions of interest for energy purposes: biomethane steam reforming and CO_2 hydrogenation. The catalysts were prepared on a zeolite with Si/Al = 385 by incipient wet impregnation at different Ni loadings.

Physico-chemical characterizations suggest the presence of hierarchical porosity with micropores (8.8 Å) and large mesopores, the latter hosting Ni nanoparticles. Catalytic results suggest that internal mass transfer limitations occur due to slow Knudsen diffusion inside the USY micropores.

The dimensions of Ni nanoparticles depend on the Ni loading. At high loadings (Ni20) large particles are detected, while at lower loadings small particles are formed. Catalytic results suggest a structure sensitivity of both reactions. In particular, steam reforming is activated by small Ni nanoparticles and Ni20 is inactive towards this reaction. The activity of the other samples towards SR increases by increasing the Ni content in the catalyst; the behaviour is less than linear due to the lower Ni dispersion on Ni10 with respect to Ni5. On the contrary, all the samples are active towards CO_2 hydrogenation; however, the structure sensitivity of this reaction affects the products distribution. As a matter of fact, large Ni nanoparticles detected on Ni20 are active towards methanation, while smaller Ni nanoparticles in Ni5 and Ni10 do not produce methane but are active towards reverse water gas shift.

Post-reaction characterizations revealed the almost complete absence of coke, suggesting a good resistance to fouling of Ni/USY catalysts. This is due to the low acidity of these samples, as suggested by

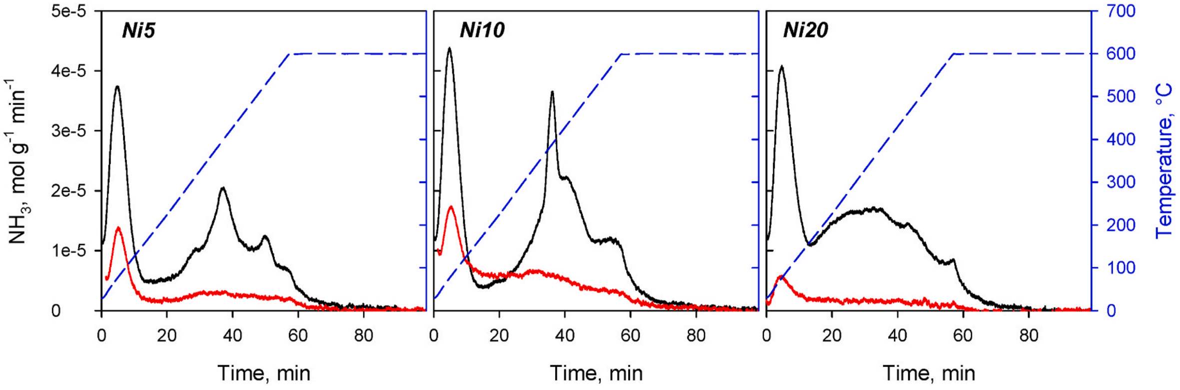

Fig. 9. TPD analysis of fresh (black lines) and used (red lines) Ni5, Ni10, and Ni20 samples; dashed lines show temperature profiles. (For interpretation of the references to colour in this figure legend, the reader is referred to the Web version of this article.)

Table 6
NH_3 desorption (mmol/g) for all tested samples.

	Ni5		Ni10		Ni20	
	Fresh	Used	Fresh	Used	Fresh	Used
Peak 1	$1.55 \bullet 10^{-1}$	$4.51 \bullet 10^{-2}$	$1.86 \bullet 10^{-1}$	$3.97 \bullet 10^{-2}$	$1.68 \bullet 10^{-1}$	$3.07 \bullet 10^{-2}$
Peak 2	$1.85 \bullet 10^{-1}$		$4.04 \bullet 10^{-2}$		$2.87 \bullet 10^{-1}$	
Peak 3	$5.51 \bullet 10^{-2}$		$3.40 \bullet 10^{-1}$			
Peak 4	$1.83 \bullet 10^{-2}$		$7.26 \bullet 10^{-2}$			
Overall	$4.13 \bullet 10^{-1}$	$4.51 \bullet 10^{-2}$	$6.39 \bullet 10^{-1}$	$3.97 \bullet 10^{-2}$	$4.55 \bullet 10^{-1}$	$3.07 \bullet 10^{-2}$

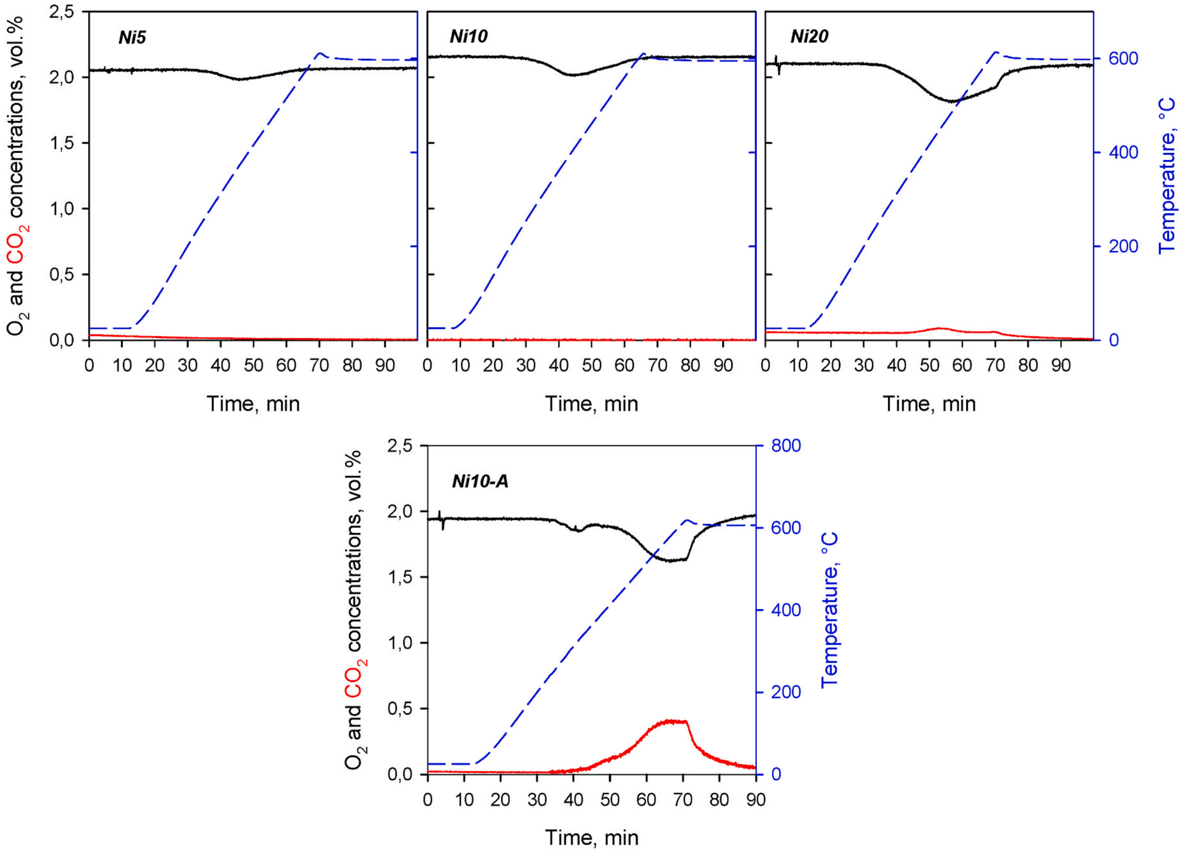

Fig. 10. CO_2 production and O_2 consumption during TPO analysis.

NH_3-TPD.

Finally, the Ni/USY catalysts do not show performance comparable to those of an alumina-supported Ni catalyst but are more resistant to fouling. It is wort noting that composition and preparation of Ni/USY catalysts are not optimized; future work will be devoted to improving the performance while keeping the anti-coking features.

CRediT authorship contribution statement

G. Sorbino: Visualization, Validation, Investigation, Data curation. **O. Tammaro:** Investigation, Data curation. **A. Padua:** Investigation. **A. Basco:** Writing – original draft, Validation, Investigation. **S. Scognamiglio:** Writing – original draft, Visualization, Investigation, Data curation. **M. Sisti:** Formal analysis. **R. Arletti:** Visualization, Formal analysis. **A. Marocco:** Investigation. **M. Pansini:** Writing – review & editing, Methodology. **G. Landi:** Writing – review & editing, Supervision, Project administration, Methodology, Funding acquisition, Conceptualization. **S. Esposito:** Writing – review & editing, Supervision, Project administration, Methodology.

Declaration of competing interest

The authors declare that they have no known competing financial interests or personal relationships that could have appeared to influence the work reported in this paper.

Acknowledgements

This work was partially funded by the Ministry of University and Research (Italy) (MUR) - Progetti di Ricerca Scientifica di Rilevante Interesse Nazionale 2020 - within the project “PLUG-IN - Process for Low-carbon blUe & green hydrogen Generation via Intensified electrified reforming of Natural gas/biogas”, Nr. 2020N38E75.

Furthermore, the Research Agreement (POR)-PNRR – “Hydrogen Research - Mission M2-C2 - Investment 3.5: Research and Development on Hydrogen, WP1 - LA1.1.25: Material and catalytic processes development for the reforming of biogas to hydrogen”, funded by the Italian Ministry of Ecological Transition (MITE) is particularly acknowledged for funding also part of this work.

Finally, A. Basco and S. Scognamiglio thank the Project funded by the European Union – NextGenerationEU under the National Recovery and

Resilience Plan (NRRP), Mission 4 “Education and Research” - Component 2 “From research to business” - Investment 3.1 “Fund for the realization of an integrated system of research and innovation infrastructures” - Call n. 3264 of December 28, 2021 of Italian Ministry of University and Research | Award Decree n. 128 (June 21, 2022) - Project code: IR0000027 - CUP: B33C22000710006 - Project title: iENTRANCE@ENL: Infrastructure for Energy TRAnsition aNd Circular Economy @ EuroNanoLab.

The authors gratefully acknowledge Mr. Andrea Capuozzo and Mr. Luigi Stanzione for XRF measurements.

Transmission Electron Microscope (TEM) was purchased with funding from the Ministry of University and Research (Italy) (MUR) under the “Dipartimento di Eccellenza 2018–2022″ program.

Dr. Marco Allione is cordially acknowledged for the experimental TEM support given for the realization of the present study.

Appendix A. Supplementary data

Supplementary data to this article can be found online at https://doi.org/10.1016/j.ijhydene.2025.01.244.

References

[1] Zainal BS, Ker PJ, Mohamed H, Ong HC, Fattah IMR, Rahman SMA, et al. Recent advancement and assessment of green hydrogen production technologies. Renew Sustain Energy Rev 2024;189:113941. https://doi.org/10.1016/j.rser.2023.113941.

[2] Zhang H, Sun Z, Hu YH. Steam reforming of methane: current states of catalyst design and process upgrading. Renew Sustain Energy Rev 2021;149:111330. https://doi.org/10.1016/j.rser.2021.111330.

[3] Iulianelli A, Liguori S, Wilcox J, Basile A. Advances on methane steam reforming to produce hydrogen through membrane reactors technology: a review. Catal Rev Sci Eng 2016;58:1–35. https://doi.org/10.1080/01614940.2015.1099882.

[4] Villora-Picó JJ, González-Arias J, Pastor-Pérez L, Odriozola JA, Reina TR. A review on high-pressure heterogeneous catalytic processes for gas-phase CO2 valorization. Environ Res 2024;240:117520. https://doi.org/10.1016/j.envres.2023.117520.

[5] Torres-Sempere G, Pastor-Perez L, Odriozola JA, Yu J, Duran-Olivencia FJ, Bobadilla LF, et al. Recent advances on gas-phase CO2 conversion: catalysis design and chemical processes to close the carbon cycle. Curr Opin Green Sustainable Chem 2022;36:100647. https://doi.org/10.1016/j.cogsc.2022.100647.

[6] Murena F, Esposito S, Deorsola FA, Galletti C, Prati MV. CO2 abatement and CH4 recovery at vehicle exhausts: comparison and characterization of Ru powder and pellet catalysts. Int J Hydrogen Energy 2020;45:8640–8. https://doi.org/10.1016/J.IJHYDENE.2020.01.120.

[7] Estevez R, Aguado-Deblas L, Bautista FM, López-Tenllado FJ, Romero AA, Luna D. A review on green hydrogen valorization by heterogeneous catalytic hydrogenation of captured CO2 into value-added products. Catalysts 2022;12:1555. https://doi.org/10.3390/catal12121555.

[8] Zhang H, Sun Z, Hu YH. Steam reforming of methane: current states of catalyst design and process upgrading. Renew Sustain Energy Rev 2021;149:111330. https://doi.org/10.1016/j.rser.2021.111330.

[9] Hasnain SMW ul, Farooqi AS, Ayodele BV, Farooqi AS, Sanaullah K, Abdullah B. Advancements in Ni and Co-based catalysts for sustainable syngas production via Bi-reforming of methane: a review of recent advances. J Clean Prod 2024;434:139904. https://doi.org/10.1016/J.JCLEPRO.2023.139904.

[10] Wang S, Nabavi SA, Clough PT. A review on bi/polymetallic catalysts for steam methane reforming. Int J Hydrogen Energy 2023;48:15879–93. https://doi.org/10.1016/J.IJHYDENE.2023.01.034.

[11] Yusuf BO, Umar M, Kotob E, Abdulhakam A, Taialla OA, Awad MM, et al. Recent advances in bimetallic catalysts for methane steam reforming in hydrogen production: current trends, challenges, and future prospects. Chem Asian J 2023;2023:e202300641. https://doi.org/10.1002/ASIA.202300641.

[12] De Souza VP, Costa D, Dos Santos D, Sato AG, Bueno JMC. Pt-promoted α-Al 2O 3-supported Ni catalysts: effect of preparation conditions on oxi-reduction and catalytic properties for hydrogen production by steam reforming of methane. Int J Hydrogen Energy 2012;37:9985–93. https://doi.org/10.1016/j.ijhydene.2012.03.141.

[13] Zhou L, Guo Y, Chen J, Sakurai M, Kameyama H. Trace precious metal Pt doped plate-type anodic alumina Ni catalysts for methane reforming reaction. Fuel 2012;92:373–6. https://doi.org/10.1016/j.fuel.2011.06.039.

[14] Baek SC, Jun KW, Lee YJ, Kim JD, Park DY, Lee KY. Ru/Ni/MgAl 2O 4 catalysts for steam reforming of methane: effects of Ru content on self-activation property. Res Chem Intermed 2012;38:1225–36. https://doi.org/10.1007/s11164-011-0462-0.

[15] Morales-Cano F, Lundegaard LF, Tiruvalam RR, Falsig H, Skjøth-Rasmussen MS. Improving the sintering resistance of Ni/Al2O3 steam-reforming catalysts by promotion with noble metals. Appl Catal Gen 2015;498:117–25. https://doi.org/10.1016/j.apcata.2015.03.016.

[16] Lee SM, Hong SC. Effect of palladium addition on catalytic activity in steam methane reforming over Ni-YSZ porous membrane. Int J Hydrogen Energy 2014;39:21037–43. https://doi.org/10.1016/j.ijhydene.2014.10.054.

[17] de Oliveira Rocha K, Marques CMP, Bueno JMC. Effect of Au doping of Ni/Al2O3 catalysts used in steam reforming of methane: mechanism, apparent activation energy, and compensation effect. Chem Eng Sci 2019;207:844–52. https://doi.org/10.1016/j.ces.2019.06.049.

[18] Wang H, Blaylock DW, Dam AH, Liland SE, Rout KR, Zhu YA, et al. Steam methane reforming on a Ni-based bimetallic catalyst: density functional theory and experimental studies of the catalytic consequence of surface alloying of Ni with Ag. Catal Sci Technol 2017;7:1713–25. https://doi.org/10.1039/c7cy00101k.

[19] Xu Y, Fan C, Zhu YA, Li P, Zhou XG, Chen D, et al. Effect of Ag on the control of Ni-catalyzed carbon formation: a density functional theory study. Catal Today 2012;186:54–62. https://doi.org/10.1016/j.cattod.2011.08.041.

[20] Nazari M, Alavi SM. An investigation of the simultaneous presence of Cu and Zn in different Ni/Al2O3 catalyst loads using Taguchi design of experiment in steam reforming of methane. Int J Hydrogen Energy 2020;45:691–702. https://doi.org/10.1016/j.ijhydene.2019.10.224.

[21] Li MR, Lu Z, Wang GC. The effect of potassium on steam-methane reforming on the Ni4/Al2O3 surface: a DFT study. Catal Sci Technol 2017;7:3613–25. https://doi.org/10.1039/c7cy00986k.

[22] Gubareni IV, Kurilets YP, Soloviev SO. Effect of additives La2O3 and CeO2 on the activity and selectivity of Ni-Al2O3/cordierite catalysts in steam reforming of methane. Theor Exp Chem 2014;50:311–7. https://doi.org/10.1007/s11237-014-9381-7.

[23] Ighalo JO, Amama PB. Recent advances in the catalysis of steam reforming of methane (SRM). Int J Hydrogen Energy 2024;51:688–700. https://doi.org/10.1016/J.IJHYDENE.2023.10.177.

[24] Al-Fatesh AS, Hanan atia, Ibrahim AA, Fakeeha AH, Singh SK, Labhsetwar NK, et al. CO2 reforming of CH4: effect of Gd as promoter for Ni supported over MCM-41 as catalyst. Renew Energy 2019;140:658–67. https://doi.org/10.1016/j.renene.2019.03.082.

[25] Nisa KS, Suendo V, Sophiana IC, Susanto H, Kusumaatmaja A, Nishiyama N, et al. Effect of base promoter on activity of MCM-41-supported nickel catalyst for hydrogen production via dry reforming of methane. Int J Hydrogen Energy 2022;47:23201–12. https://doi.org/10.1016/j.ijhydene.2022.05.081.

[26] Fakeeha AH, Kasim SO, Ibrahim AA, Abasaeed AE, Al-Fatesh AS. Influence of nature support on methane and CO2 conversion in a dry reforming reaction over nickel-supported catalysts. Materials 2019;12:1777. https://doi.org/10.3390/ma12111777.

[27] Jeong H, Kim KI, Kim D, Song IK. Effect of promoters in the methane reforming with carbon dioxide to synthesis gas over Ni/HY catalysts. J Mol Catal Chem 2006;246:43–8. https://doi.org/10.1016/j.molcata.2005.10.013.

[28] Siang TJ, Bach LG, Singh S, Truong QD, Ho VTT, Huy Phuc NH, et al. Methane bi-reforming over boron-doped Ni/SBA-15 catalyst: longevity evaluation. Int J Hydrogen Energy 2019:20839–50. https://doi.org/10.1016/j.ijhydene.2018.06.123.

[29] Rossetti I, Bonelli B, Ramis G, Bahadori E, Nasi R, Aronne A, et al. New insights into the role of the synthesis procedure on the performance of Co-based catalysts for ethanol steam reforming. Top Catal 2018;61:1734–45. https://doi.org/10.1007/S11244-018-0969-3/TABLES/3.

[30] Rönsch S, Schneider J, Matthischke S, Schlüter M, Götz M, Lefebvre J, et al. Review on methanation – from fundamentals to current projects. Fuel 2016;166:276–96. https://doi.org/10.1016/J.FUEL.2015.10.111.

[31] Parizotto NV, Rocha KO, Damyanova S, Passos FB, Zanchet D, Marques CMP, et al. Alumina-supported Ni catalysts modified with silver for the steam reforming of methane: effect of Ag on the control of coke formation. Appl Catal Gen 2007;330:12–22. https://doi.org/10.1016/J.APCATA.2007.06.022.

[32] Borowiecki T, Denis A, Rawski M, Gołębiowski A, Stołecki K, Dmytrzyk J, et al. Studies of potassium-promoted nickel catalysts for methane steam reforming: effect of surface potassium location. Appl Surf Sci 2014;300:191–200. https://doi.org/10.1016/J.APSUSC.2014.02.053.

[33] Ma Y, Liu J, Chu M, Yue J, Cui Y, Xu G. Cooperation between active metal and basic support in Ni-based catalyst for low-temperature CO2 methanation. Catal Lett 2020;150:1418–26. https://doi.org/10.1007/S10562-019-03033-W/FIGURES/5.

[34] Sholeha NA, Mohamad S, Bahruji H, Prasetyoko D, Widiastuti N, Abdul Fatah NA, et al. Enhanced CO2methanation at mild temperature on Ni/zeolite from kaolin: effect of metal-support interface. RSC Adv 2021;11:16376–87. https://doi.org/10.1039/d1ra01014j.

[35] Guo X, Traitangwong A, Hu M, Zuo C, Meeyoo V, Peng Z, et al. Carbon dioxide methanation over nickel-based catalysts supported on various mesoporous material. Energy Fuel 2018;32:3681–9. https://doi.org/10.1021/acs.energyfuels.7b03826.

[36] Quatorze IF, Gonçalves LPL, Kolen’ko YV, Soares OSGP, Pereira MFR. CO2 methanation over Ni supported on Carbon–ZrO2: an optimization of the composite composition. Catal Today 2023;422:114215. https://doi.org/10.1016/j.cattod.2023.114215.

[37] da Costa-Serra JF, Cerdá-Moreno C, Chica A. Zeolite-supported Ni catalysts for CO2 methanation: effect of zeolite structure and Si/Al ratio. Appl Sci 2020;10. https://doi.org/10.3390/app10155131.

[38] Tommasi M, Degerli SN, Ramis G, Rossetti I. Advancements in CO2 methanation: a comprehensive review of catalysis, reactor design and process optimization.

Chem Eng Res Des 2024;201:457–82. https://doi.org/10.1016/J.CHERD.2023.11.060.

[39] Fakeeha AH, Kasim SO, Ibrahim AA, Abasaeed AE, Al-Fatesh AS. Influence of nature support on methane and CO2 conversion in a dry reforming reaction over nickel-supported catalysts. Materials 2019;12:1777. https://doi.org/10.3390/ma12111777.

[40] Mierczynski P, Mosinska M, Stepinska N, Chalupka K, Nowosielska M, Maniukiewicz W, et al. Effect of the support composition on catalytic and physicochemical properties of Ni catalysts in oxy-steam reforming of methane. Catal Today 2021;364:46–60. https://doi.org/10.1016/j.cattod.2020.05.037.

[41] Gopalakrishnan S, Faga MG, Miletto I, Coluccia S, Caputo G, Sau S, et al. Unravelling the structure and reactivity of supported Ni particles in Ni-CeZrO2 catalysts. Appl Catal, B 2013;138–139:353–61. https://doi.org/10.1016/j.apcatb.2013.02.036.

[42] Yasuda S, Osuga R, Kunitake Y, Kato K, Fukuoka A, Kobayashi H, et al. Zeolite-supported ultra-small nickel as catalyst for selective oxidation of methane to syngas. Commun Chem 2020;3:1–8. https://doi.org/10.1038/s42004-020-00375-0.

[43] Nieva MA, Villaverde MM, Monzón A, Garetto TF, Marchi AJ. Steam-methane reforming at low temperature on nickel-based catalysts. Chem Eng J 2014;235:158–66. https://doi.org/10.1016/J.CEJ.2013.09.030.

[44] Wei L, Haije W, Kumar N, Peltonen J, Peurla M, Grenman H, et al. Influence of nickel precursors on the properties and performance of Ni impregnated zeolite 5A and 13X catalysts in CO2 methanation. Catal Today 2021;362:35–46. https://doi.org/10.1016/j.cattod.2020.05.025.

[45] Sholeha NA, Mohamad S, Bahruji H, Prasetyoko D, Widiastuti N, Abdul Fatah NA, et al. Enhanced CO2methanation at mild temperature on Ni/zeolite from kaolin: effect of metal-support interface. RSC Adv 2021;11:16376–87. https://doi.org/10.1039/d1ra01014j.

[46] da Costa-Serra JF, Cerdá-Moreno C, Chica A. Zeolite-supported Ni catalysts for CO2 methanation: effect of zeolite structure and Si/Al ratio. Appl Sci 2020;10. https://doi.org/10.3390/app10155131.

[47] Bacariza MC, Bértolo R, Graça I, Lopes JM, Henriques C. The effect of the compensating cation on the catalytic performances of Ni/USY zeolites towards CO2 methanation. J CO2 Util 2017;21:280–91. https://doi.org/10.1016/j.jcou.2017.07.020.

[48] Hu F, Ye R, Jin C, Liu D, Chen X, Li C, et al. Ni nanoparticles enclosed in highly mesoporous nanofibers with oxygen vacancies for efficient CO2 methanation. Appl Catal, B 2022;317:121715. https://doi.org/10.1016/j.apcatb.2022.121715.

[49] Grzybek G, Greluk M, Tarach K, Pyra K, Słowik G, Rotko M, et al. Bioethanol steam reforming over cobalt-containing USY and ZSM-5 commercial zeolite catalysts. Front Mater 2020;7:597528. https://doi.org/10.3389/FMATS.2020.597528/BIBTEX.

[50] Frontera P, Aloise A, MacArio A, Crea F, Antonucci PL, Giordano G, et al. Zeolite-supported Ni catalyst for methane reforming with carbon dioxide. Res Chem Intermed 2011;37:267–79. https://doi.org/10.1007/S11164-011-0249-3/SCHEMES/2.

[51] Baerlocher C, McCusker LB, Olson DH. Atlas of zeolite framework types. Atlas of zeolite framework types. sixth ed. 2007. p. 1–398. https://doi.org/10.1016/B978-0-444-53064-6.X5186-X. Sixth Edition.

[52] Gualtieri AF, Mazzucato E, Venturelli P, Viani A, Zannini P, Petras L. X-ray powder diffraction quantitative analysis performed in situ at high temperature: application to the determination of NiO in ceramic pigments. J Appl Crystallogr 1999;32:808–13. https://doi.org/10.1107/S0021889899005853.

[53] Toby BH. EXPGUI, a graphical user interface for GSAS. J Appl Crystallogr 2001;34:210–3. https://doi.org/10.1107/S0021889801002242/HTTPS://JOURNALS.IUCR.ORG/SERVICES/TERMSOFUSE.HTML.

[54] Larson AC, Von RB, Lansce D. General structure analysis system (GSAS). 2004.

[55] Parise JB, Corbin DR, Abrams L, Cox DE. Structure of dealuminated Linde Y-zeolite; Si139.7Al52.3O384 and Si173.1Al18.9O384: presence of non-framework Al species, vol. 40. Urn:Issn; 1984. p. 1493–7. https://doi.org/10.1107/S0108270184008490.

[56] Pansini M, Dell'Agli G, Marocco A, Netti PA, Battista E, Lettera V, et al. Preparation and characterization of magnetic and porous metal-ceramic nanocomposites from a zeolite precursor and their application for DNA separation. J Biomed Nanotechnol 2017;13:337–48. https://doi.org/10.1166/JBN.2017.2345.

[57] Luciani G, Landi G, Aronne A, Di Benedetto A. Partial substitution of B cation in La0.6Sr0.4MnO3 perovskites: a promising strategy to improve the redox properties useful for solar thermochemical water and carbon dioxide splitting. Sol Energy 2018;171:1–7. https://doi.org/10.1016/j.solener.2018.06.058.

[58] Bagnasco G, Cammarano C, Turco M, Esposito S, Aronne A, Pernice P. TPR/TPO characterization of cobalt–silicon mixed oxide nanocomposites prepared by sol–gel. Thermochim Acta 2008;471:51–4. https://doi.org/10.1016/J.TCA.2008.02.019.

[59] Portarapillo M, Russo D, Landi G, Luciani G, Di Benedetto A. K-doped CeO 2 –ZrO 2 for CO 2 thermochemical catalytic splitting. RSC Adv 2021;11:39420–7. https://doi.org/10.1039/d1ra08315e.

[60] Di Benedetto A, Landi G, Lisi L. Improved CO-prox performance of CuO/CeO2 catalysts by using nanometric ceria as support. Catalysts 2018;8:209. https://doi.org/10.3390/catal8050209.

[61] Satterfield CN, Sherwood TK. The role of diffusion in catalysis. Addison-Wesley Pub. Co.; 1963.

[62] Landi G, Barbato PS, Di Benedetto A, Pirone R, Russo G. High pressure kinetics of CH4, CO and H2 combustion over LaMnO3 catalyst. Appl Catal, B 2013;134–135:110–22. https://doi.org/10.1016/j.apcatb.2012.12.040.

[63] Robinson AM, Gin ME, Yung MM. Methane steam reforming kinetics on a Ni/Mg/K/Al2O3 catalyst. Top Catal 2013;56:1708–15. https://doi.org/10.1007/s11244-013-0106-2. Springer.

[64] Nielsen M, Hafreager A, Brogaard RY, De Wispelaere K, Falsig H, Beato P, et al. Collective action of water molecules in zeolite dealumination. Catal Sci Technol 2019;9:3721–5. https://doi.org/10.1039/c9cy00624a.

[65] Khosravani H, Meshksar M, Koohi-Saadi M, Taghadom K, Rahimpour MR. Synthesis, characterization, and application of bio-templated Ni–Ce/Al2O3 catalyst for clean H2 production in the steam reforming of methane process. J Energy Inst 2023;108:101203. https://doi.org/10.1016/j.joei.2023.101203.

[66] Nazari M, Alavi SM. An investigation of the simultaneous presence of Cu and Zn in different Ni/Al2O3 catalyst loads using Taguchi design of experiment in steam reforming of methane. Int J Hydrogen Energy 2020;45:691–702. https://doi.org/10.1016/j.ijhydene.2019.10.224.

[67] Sebai I, Boulahaouache A, Trari M, Salhi N. Preparation and characterization of 5%Ni/Γ-Al2o3 catalysts by complexation with NH3 derivatives active in methane steam reforming. Int J Hydrogen Energy 2019;44:9949–58. https://doi.org/10.1016/j.ijhydene.2018.12.050.

[68] Azancot L, Bobadilla LF, Santos JL, Córdoba JM, Centeno MA, Odriozola JA. Influence of the preparation method in the metal-support interaction and reducibility of Ni-Mg-Al based catalysts for methane steam reforming. Int J Hydrogen Energy 2019;44:19827–40. https://doi.org/10.1016/j.ijhydene.2019.05.167.

[69] Yang X, Da J, Yu H, Wang H. Characterization and performance evaluation of Ni-based catalysts with Ce promoter for methane and hydrocarbons steam reforming process. Fuel 2016;179:353–61. https://doi.org/10.1016/j.fuel.2016.03.104.

[70] Guo X, Traitangwong A, Hu M, Zuo C, Meeyoo V, Peng Z, et al. Carbon dioxide methanation over nickel-based catalysts supported on various mesoporous material. Energy Fuel 2018;32:3681–9. https://doi.org/10.1021/acs.energyfuels.7b03826.

[71] Ranjbar A, Irankhah A, Aghamiri SF. Reverse water gas shift reaction and CO2 mitigation: nanocrystalline MgO as a support for nickel based catalysts. J Environ Chem Eng 2018;6:4945–52. https://doi.org/10.1016/j.jece.2018.07.032.

[72] Liu N, Cui S, Jin Z, Cao Z, Liu H, Yang S, et al. Highly dispersed and stable Ni/SiO2 catalysts prepared by urea-assisted impregnation method for reverse water–gas shift reaction. Processes 2023;11. https://doi.org/10.3390/pr11051353.

[73] Gioria E, Ingale P, Pohl F, Naumann d'Alnoncourt R, Thomas A, Rosowski F. Boosting the performance of Ni/Al2O3 for the reverse water gas shift reaction through formation of CuNi nanoalloys. Catal Sci Technol 2022;12:474–87. https://doi.org/10.1039/d1cy01585k.

[74] Huang C, Li A, Chao ZS. Heterogeneous catalytic synthesis of quinoline compounds from aniline and C1–C4 alcohols over zeolite-based catalysts. RSC Adv 2017;7:48275–85. https://doi.org/10.1039/C7RA08442K.

[75] Aumond T, Rousseau J, Pouilloux Y, Pinard L, Sachse A. Synthesis of hierarchical zeolite templated carbons. Carbon Trends 2021;2:100014. https://doi.org/10.1016/J.CARTRE.2020.100014.

[76] Tammaro O, Morante N, Marocco A, Fontana M, Castellino M, Barrera G, et al. The beneficial role of nano-sized Fe3O4 entrapped in ultra-stable Y zeolite for the complete mineralization of phenol by heterogeneous photo-Fenton under solar light. Chemosphere 2023;345:140400. https://doi.org/10.1016/J.CHEMOSPHERE.2023.140400.

[77] Da Costa-Serra JF, Navarro MT, Rey F, Chica A. Bioethanol steam reforming on Ni-based modified mordenite. Effect of mesoporosity, acid sites and alkaline metals. Int J Hydrogen Energy 2012;37:7101–8. https://doi.org/10.1016/J.IJHYDENE.2011.10.086.

[78] Chai Y, Shang W, Li W, Wu G, Dai W, Guan N, et al. Noble metal particles confined in zeolites: synthesis, characterization, and applications. Adv Sci 2019;6:1900299. https://doi.org/10.1002/ADVS.201900299.

[79] Xu J, Yin T, Li Y, Liu N, Shi L, Meng X. Synthesis of high hydrophobicity USY zeolite with excellent VOCs adsorption performance under humid condition: combined strategy of high temperature steam and acid treatment. Sep Purif Technol 2024;329:124914. https://doi.org/10.1016/J.SEPPUR.2023.124914.

[80] Pang H, Yang G, Li L, Yu J. Toward the production of renewable diesel over robust Ni nanoclusters highly dispersed on a two-dimensional zeolite n.d. https://doi.org/10.1038/s41427-023-00471-2.

[81] Tammaro O, Barrera G, Allia P, Tiberto P, Marocco A, Manzoli M, et al. Unravelling the role of the exchanged Ni amount in zeolites A and X for their thermal transformation into magnetic metal-ceramic nanocomposites. Ceram Int 2023;49:30536–46. https://doi.org/10.1016/J.CERAMINT.2023.07.003.

[82] Spataru D, Canastreiro D, Świrk Da Costa K, Quindimil A, Lopes JM, Da Costa P, et al. Doping Ni/USY zeolite catalysts with transition metals for CO2 methanation. Int J Hydrogen Energy 2024;53:468–81. https://doi.org/10.1016/J.IJHYDENE.2023.12.045.

[83] Esposito S, Silvestri B, Russo V, Bonelli B, Manzoli M, Deorsola FA, et al. Self-activating catalyst for glucose hydrogenation in the aqueous phase under mild conditions. ACS Catal 2019;9:3426–36. https://doi.org/10.1021/ACSCATAL.8B04710/SUPPL_FILE/CS8B04710_SI_001.PDF.

[84] De Jong KP, Zečević J, Friedrich H, De Jongh PE, Bulut M, Van Donk S, et al. Zeolite y crystals with trimodal porosity as ideal hydrocracking catalysts. Angew Chem Int Ed 2010;49:10074–8. https://doi.org/10.1002/ANIE.201004360.

[85] Hartmann M, Machoke AG, Schwieger W. Catalytic test reactions for the evaluation of hierarchical zeolites. Chem Soc Rev 2016;45:3313–30. https://doi.org/10.1039/C5CS00935A.

[86] Verboekend D, Vilé G, Pérez-Ramírez J. Hierarchical Y and USY zeolites designed by post-synthetic strategies. Adv Funct Mater 2012;22:916–28. https://doi.org/10.1002/ADFM.201102411.

[87] Wei Y, Feng J, Guan B, Yu J. Structural engineering of hierarchical zeolite-based catalysts. Acc Mater Res 2024. https://doi.org/10.1021/ACCOUNTSMR.4C00076/ASSET/IMAGES/LARGE/MR4C00076_0009.JPEG.

[88] Vogt C, Kranenborg J, Monai M, Weckhuysen BM. Structure sensitivity in steam and dry methane reforming over nickel: activity and carbon formation. ACS Catal 2020;10:1428–38. https://doi.org/10.1021/acscatal.9b04193.

[89] Hu F, Ye R, Lu ZH, Zhang R, Feng G. Structure-activity relationship of Ni-based catalysts toward CO2Methanation: recent advances and future perspectives. Energy Fuel 2022;36:156–69. https://doi.org/10.1021/acs.energyfuels.1c03645.

[90] Tian X, Wei Y, Zhao H. Evaluation of a hierarchically-structured CuO@TiO2-Al2O3oxygen carrier for chemical looping with oxygen uncoupling. Fuel 2017;209:402–10. https://doi.org/10.1016/j.fuel.2017.08.022.

[91] García-Bordejé E, Liu Y, Su DS, Pham-Huu C. Hierarchically structured reactors containing nanocarbons for intensification of chemical reactions. J Mater Chem A Mater 2017;5:22408–41. https://doi.org/10.1039/c7ta06826c.

[92] Szymańska K, Odrozek K, Zniszczoł A, Pudło W, Jarzębski AB. A novel hierarchically structured siliceous packing to boost the performance of rotating bed enzymatic reactors. Chem Eng J 2017;315:18–24. https://doi.org/10.1016/j.cej.2016.12.131.

[93] Moon DS, Lee JK. Tunable synthesis of hierarchical mesoporous silica nanoparticles with radial wrinkle structure. Langmuir 2012;28:12341–7. https://doi.org/10.1021/la302145j.

[94] Miguel-García I, Navlani-García M, García-Aguilar J, Berenguer-Murcia Á, Lozano-Castelló D, Cazorla-Amorós D. Capillary microreactors based on hierarchical SiO_2 monoliths incorporating noble metal nanoparticles for the Preferential Oxidation of CO. Chem Eng J 2015;275:71–8. https://doi.org/10.1016/j.cej.2015.04.020.

[95] Ding S, Ganesh M, Jiao Y, Ou X, Isaacs MA, S'Ari M, et al. Palladium-doped hierarchical ZSM-5 for catalytic selective oxidation of allylic and benzylic alcohols. R Soc Open Sci 2021;8. https://doi.org/10.1098/rsos.211086.

[96] Silva TQ, dos Santos MB, Santiago AAC, Santana DO, Cruz FT, Andrade HMC, et al. Gas phase glycerol oxidative dehydration over bifunctional V/H-zeolite catalysts with different zeolite topologies. Catal Today 2017;289:38–46. https://doi.org/10.1016/j.cattod.2016.08.011.

[97] Chatla A, Almanassra IW, Kallem P, Atieh MA, Alawadhi H, Akula V, et al. Dry (CO2) reforming of methane over zirconium promoted Ni-MgO mixed oxide catalyst: effect of Zr addition. J CO2 Util 2022;62:102082. https://doi.org/10.1016/j.jcou.2022.102082.

[98] Gao X, Li J, Zheng M, Cai S, Zhang J, Askari S, et al. Recent progress in anti-coking Ni catalysts for thermo-catalytic conversion of greenhouse gases. Process Saf Environ Protect 2021;156:598–616. https://doi.org/10.1016/J.PSEP.2021.10.051.

[99] Lee SU, Lee YJ, Kwon SJ, Kim JR, Jeong SY. Pt-Sn supported on beta zeolite with enhanced activity and stability for propane dehydrogenation. Catalysts 2021;11. https://doi.org/10.3390/CATAL11010025. Page 25 2020;11:25.

[100] Tamura K, Murata D, Sumi T, Kokuryo S, Kitamura H, Tsubota S, et al. Dry reforming of methane with suppressed carbon deposition over Cr- and Ni-loaded dealuminated β zeolites. Energy Fuel 2023;37:18945–51. https://doi.org/10.1021/ACS.ENERGYFUELS.3C02837/ASSET/IMAGES/LARGE/EF3C02837_0006.JPEG.

[101] Elnour AY, Fakeeha AH, Ibrahim AA, Osman AI, Abasaeed AE, Adil SF, et al. Enhancing catalytic performance, coke resistance, and stability with strontium-promoted Ni/WO3-ZrO2 catalysts for methane dry reforming. Res Chem Intermed 2024;50:1211–30. https://doi.org/10.1007/S11164-023-05210-4/FIGURES/9.

[102] Song G, Li C, Zhou W, Wu L, Lim KH, Hu F, et al. Catalytic decomposition of methane for controllable production of carbon nanotubes and high purity H2 over LTA zeolite-derived Ni-based yolk-shell catalysts. Chem Eng J 2023;474:145643. https://doi.org/10.1016/J.CEJ.2023.145643.

[103] Serrano DP, Botas JA, Pizarro P, Moreno I, Gómez G. Hydrogen production through catalytic methane decomposition promoted by pure silica materials. Int J Hydrogen Energy 2015;40:5237–43. https://doi.org/10.1016/J.IJHYDENE.2015.01.056.